

Modeling Shallow Water Flows on General Terrains

Ilaria Fent^{a,*}, Mario Putti^b, Carlo Gregoretti^c, Stefano Lanzoni^d

^a *Institute of Mechanics, Materials and Civil Engineering, Université Catholique de Louvain, Belgium*

^b *Department of Mathematics, University of Padua, Italy*

^c *Department of Land, Environment, Agriculture and Forestry, University of Padua, Italy*

^d *Department of Civil, Environmental and Architectural Engineering, University of Padua, Italy*

Abstract

A formulation of the two-dimensional shallow water equations adapted to general and complex terrains is proposed. Its derivation starts from the observation that the typical approach of depth integrating the Navier-Stokes equations along the direction of gravity forces is not exact in the general case of a tilted curved bottom. We claim that an integration path that better adapts to the shallow water hypotheses follows the “cross-flow” surface, i.e., a surface that is normal to the velocity field at any point of the domain. Because of the implicitness of this definition, we approximate this “cross-flow” path by performing depth integration along a local direction normal to the bottom surface, and propose a rigorous derivation of this approximation and its numerical solution as an essential step for the future development of the full “cross-flow” integration procedure. We start by defining a local coordinate system, anchored on the bottom surface to derive a covariant form of the Navier-Stokes equations. Depth integration along the local normals yields a covariant version of the shallow water equations, which is characterized by flux functions and source terms that vary in space because of the surface metric coefficients and related derivatives. The proposed model is numerically discretized with a first order FORCE-type Godunov Finite Volume scheme that allows straight forward implementation of spatially variable fluxes. We investigate the validity of our SW model and the effects of the geometrical characteristics of the bottom surface by means of three synthetic test cases that exhibit non negligible slopes and surface curvatures. The results show the importance of taking into consideration bottom geometry even for relatively mild and slowly varying curvatures. By comparison with the numerical solution of vertically integrated models, we observe differences of almost 20%, in particular for the peak values and the shape of the hydrographs calculated at given sections of the fluid domain.

Keywords: Shallow Water, General topography, Curvature effects, Finite Volumes

1. Introduction

Shallow Water Equations (SWE) are classically used as models of environmental fluid dynamics when the flow field has one component that is negligible with respect to the other two, e.g., the vertical velocity component is small with respect to the horizontal (longitudinal and lateral) components. This is the so called Shallow Water (SW) hypothesis, and is considered true when the process has a dominant characteristic dimension. Applications of SWE range from large-scale ocean modeling [1] to atmospheric circulation [2], from river morphodynamics [3, 4] to dam break and granular flows [5–8], to avalanches [9]. The common derivation of this hyperbolic system of balance laws is based on the integration of the Navier-Stokes (NS) equations over the fluid depth in combination with an asymptotic analysis implementing the SW assumption [10]. For slowly varying bottom topographies fluid depth is evaluated along the vertical direction as an approximation

*Corresponding author

Email addresses: ilaria.fent@uclouvain.be (Ilaria Fent), mario.putti@unipd.it (Mario Putti), carlo.gregoretti@unipd.it (Carlo Gregoretti), stefano.lanzoni@unipd.it (Stefano Lanzoni)

of the bottom normal. This approach is generally used in modeling large scale ocean dynamics or atmospheric flows, where the bottom boundary is the geo-sphere and the normal direction coincides with the direction of gravitational forces [11]. Also at smaller scales, typical of models of river hydraulics or granular and snow avalanches, the vertical direction is ordinarily utilized [12]. However, this approximation is valid only for relatively small angles, commonly estimated at about six degrees with respect to horizontal [13], and for negligible curvatures of the bottom relief. To improve accuracy, ad hoc pressure corrections are often devised to take into account deviations of the vertical pressure profile from the hydrostatic behavior due to bathymetry variability [1]. More recent attempts look at extensions of the Boussinesq scaling approach to evaluate these corrective terms [14], employing sufficiently low order Green-Naghdi polynomial expansions of the vertical pressure profile to combine accuracy and computational efficiency of the resulting model [15]. Another recent non-hydrostatic pressure solver for the nonlinear shallow water equations proposed in [16].

For bed shapes with more general geometries, vertical integration is inaccurate and the normal to the bottom profile is preferred. Studies that attempt to quantify the accuracy of the vertical integration approximation are scarce. Perturbation approaches have been used to derive the SW equations on general topography with resulting models usually valid for low enough Reynolds numbers (Re). For example, [17, 18] model thin film flows in lubrication theory ($Re \sim 300$) to simulate instabilities that develop at long wavelengths using approaches resting on truncated gradient expansions. However, for larger values of Re typical of geophysical applications, even when considering steady flow conditions, the leading order solution poses the problem of matching together the velocity profiles in the inertial and the viscous layers [19]. In addition, not less important is the consideration of the spatial variability of the bed roughness that always characterizes geophysical flows and the ensuing uncertainty (see, e.g., [20, 21]).

Within our context of environmental fluid dynamics, the early work of [22, 23] posed the foundation for studies of non planar beds by developing a formulation of the SW model in local curvilinear coordinates based on depth integration along the normal to the topography. This approach is valid only for small and essentially one-dimensional bottom curvatures, and, in practice, it assumes that the fluid surface is parallel to the bottom. More recently, [24] extended the methodology to more general bottom surfaces, but its theoretical and practical limitations have not been extensively studied, as well as its numerical solution, although a number of applications that use this model have been published [e.g., 25, 26]. Using a different approach, [27] considered SW equations on manifolds, developing an original a modification of the wave propagation algorithm described in [28] to work on non-autonomous fluxes arising from geometrical information, and apply it to SWE on the sphere.

In this paper we derive a governing system that resembles in many ways the model of [24], but our derivation allows the direct identification of the neglected/retained terms during the enforcement of the SW assumption. This entails a better understanding of the limitations and assumptions intrinsic to the final governing PDE, include the accurate identification of the actual hypothesis on the bed geometry. Thus, the equations are written in coordinates instead of intrinsic operators with the intent of isolating the terms leading to these limitations, in order to carefully identify the correct mathematical assumptions that lead to the proposed model in covariant form.

Our developments start from the observation that, in flows over general terrains, streamlines deviate substantially from a rectilinear behavior and may assume generally curved shapes that are independent of the bed configuration. In this case, the SW hypothesis of small vertical velocity needs to be adapted to the curvilinear path of the streamlines. This adaptation can be intuitively explained as follows. We first note that the SW assumption is identically satisfied on lines that are orthogonal to the velocity vector at each point. In other words, the velocity components that are tangential to these so-called “cross-flow” lines, and that play the role of the vertical components, are always zero. If we now define a local curvilinear reference system anchored on the bottom surface and with the third direction following the cross-flow lines, we can proceed to integrate along these paths to arrive at the SW system, once the profile of the velocity normal to the cross-flow direction is assumed. A similar concept is already contained in [29]. However, the definition of cross-flow path is implicit and thus impractical as it requires the knowledge of the NS velocity field, an unknown of the problem. To solve this difficulty, [30] and [31] propose a discretization of the cross-flow path by means of a discrete Fourier transformation. The resulting model approaches the complexity of a full three-dimensional simulation. Alternatively, we may think of approximating the cross-flow lines by discretization

using piecewise linear polynomials. This leads to a multi-layer system where the cross-flow lines can be approximated with the straight direction locally normal to each layer bottom. This strategy is affected by an error that depends on the thickness of the layers and its full definition contains still some outstanding issues. In this paper we address one of them, namely the derivation of an appropriate curvilinear reference system and the definition of the SW model structure for a single layer by performing depth integration along the local normals.

The completion of the depth integration procedure requires the knowledge of the velocity variation along the integration path. In general, the shape of this profile varies with the type of fluid and flow regime. Linear, parabolic, or logarithmic approximations have been proposed with reference to the specific characteristics of the fluid (e.g., water, granular mixtures) and of the flow (e.g., laminar, turbulent, grain-inertial, quasi static). In our derivation, the departure of this profile from the depth averaged value is accounted for by adding multiplicative coefficients to the advective fluxes that take into consideration the vertical non-uniformity of cross-flow velocities. These are often called differential advection terms [32], and, in the geophysical literature, are alternatively thought of as residual dispersive stresses [33–35] and are mostly neglected [32, 36]. For all these approaches, empirical formulations accounting for bottom stresses are often employed. As shown by [10], this strategy yields solutions that are very similar to more sophisticated and rigorous developments, so that their use is strictly justified, although a-posteriori.

Note that our work is different from the so called boundary-fitted numerical schemes, typically used in atmospheric flows, where a curvilinear coordinate system follow mesh edges that are built on the boundary-following surfaces. This approach has been proposed recently for the SW equation on general topography by [37] and [38]. In this approach the authors rewrite the standard SW equation in the curvilinear coordinate system following cell boundaries. As such, the SWE do not embody all the geometric information arising from the bottom surface.

An accurate solution of the SW equations requires the analysis of the well-balance problem. Typically, corrective factors that maintain consistency of the scheme are introduced in these situations (see the booklet by [39]). Determination of these corrections is still an open question in the case of general surfaces (see [40]), and ensuring consistency is not trivial. Our choice is then to perform "exact" analytical calculations as much as possible and to resort to numerical approximations that are consistent independently of the fact that we take into account geometrical effects or not. Indeed, all our test cases are designed in such a way that well-balance errors are negligible, i.e., the fluid is always moving with enough speed.

In this work we present the development of the proposed SW model and its numerical discretization by finite volumes. By comparison on simple test cases, numerical results show that neglecting bottom curvature information leads to significant differences. We start by describing the NS equations written in covariant form with respect to a well-defined local reference system and proceed by performing depth integration along the normal defined at each point of the bottom surface. We then formulate a first order FORCE-type Godunov Finite Volume scheme for the numerical solution of the resulting equations. We borrow our formulation from the work of [41, 42] who propose a second-order FORCE-based SW solver with wetting-and-drying and well-balance properties. This approach has been tested on several standard problems and a number of real-world applications. The rationale for the use of this approach is that the FORCE scheme is based on a central flux approximation that does not require the definition of a Riemann problem. Simulations performed on synthetic but realistic test cases defined on smooth curved domains show that the influence of the bottom geometry is important even in the presence of small curvatures.

2. Equations of motion

We start this section by first writing the Navier-Stokes equations using a global Cartesian (orthogonal) reference frame. The equations are assumed to be defined in a three-dimensional domain bounded by smooth surfaces. Next, we switch our description to a local curvilinear reference system positioned on the surface defining the topography of the bottom. Then, all the developments, including depth integration, will be carried out with respect to this local reference system. A rigorous definition of this curvilinear reference system is fundamental to understand, at least qualitatively, the limitations introduced by our approximations.

A remark on notation: in the following we never use contravariant quantities but only covariant or physical components, and hence we do not use Einstein summation convention and do not indicate contravariant or covariant vectors using superscripts or subscripts, as typical of classical tensor analysis. Instead, we always report the complete expressions and definitions of all the operators and quantities used in the developments, including the summation indices and their bounds explicitly, and pointing at specialized literature if necessary.

2.1. Equations of motion in global Cartesian coordinates

The equations of motion for an incompressible fluid using a Global Cartesian Coordinate System (GCS) can be written as [43]:

$$\begin{aligned} \frac{\partial \mathbf{u}}{\partial t} + \nabla \cdot (\mathbf{u} \otimes \mathbf{u}) &= -\frac{1}{\rho} \nabla \cdot (p\mathbb{I} + \mathbb{T}) + \mathbf{g}, \\ \nabla \cdot \mathbf{u} &= 0, \end{aligned} \tag{1}$$

where \mathbf{u} is the three-dimensional velocity vector, $t \in I_T = [0, T]$ is time, ∇ indicates the gradient of a function in Cartesian coordinates, $\nabla \cdot$ is the divergence of a vector or a tensor (in this latter case $\nabla \cdot$ operates on each row of the tensor), \otimes is the tensor product of two vectors ($\mathbf{u} \otimes \mathbf{u} = \mathbf{u}\mathbf{u}^T$), ρ is the density of the fluid, p is the dynamic fluid pressure, \mathbb{I} is the identity tensor, \mathbb{T} is the deviatoric component of the turbulent stress tensor, and \mathbf{g} is the gravitational acceleration vector.

The NS equations are defined for each time t on a domain Ω , a subset of \mathbb{R}^3 with boundary $\partial\Omega$ formed by the union of three material surfaces identifying the bottom surface (\mathcal{S}_B), the fluid free surface (\mathcal{S}_W), and the lateral surface (\mathcal{S}_L). We denote with \mathbf{x} the position vector of a generic point of the domain Ω with respect to a global Cartesian (orthogonal) coordinate system spanned by the canonical basis vectors ($\mathbf{e}_1, \mathbf{e}_2, \mathbf{e}_3$):

$$\mathbf{x} = (x_1, x_2, x_3) = x_1\mathbf{e}_1 + x_2\mathbf{e}_2 + x_3\mathbf{e}_3.$$

We assume that the bottom and free surfaces are regular [44]. Mathematically speaking, a regular surface is a connected subset $\mathcal{S} \subset \mathbb{R}^3$ such that for every $\mathbf{P} \in \mathcal{S}$ there exists a \mathcal{C}^∞ map $\Psi : \mathcal{A} \mapsto \mathbb{R}^3$, with $\mathcal{A} \subset \mathbb{R}^2$, having the ensuing properties: i) there exists an open neighborhood $\mathcal{V} \subset \mathbb{R}^3$ of \mathbf{P} such that $\Psi(\mathcal{A}) = \mathcal{V} \cap \mathcal{S}$; ii) Ψ is a homeomorphism of its image; iii) the differential of Ψ in \mathbf{P} , represented by the 3×2 Jacobian matrix $d\Psi_{\mathbf{P}} = \{\partial\Psi_i/\partial x_j\}$, is injective (it has maximum rank). This definition of a surface focuses on the local properties of the map $\Psi(\mathcal{A})$ that contains all the information needed for the definition of the local coordinate system. Essentially, $\mathcal{S} \subset \mathbb{R}^3$ is a regular surface if it contains no self-intersections, every point of \mathcal{S} can be described by a continuous, differentiable, and invertible local parametrization, i.e., the map Ψ , and at each point $\mathbf{P} \in \mathcal{S}$ the tangent plane $\mathcal{T}_{\mathbf{P}}\mathcal{S}$ is well defined, or, in other words, it does not reduce to a line or a point [45].

We will identify these surfaces as the zero level set of an implicit function, and will give more precise definitions when needed:

$$\begin{aligned} \mathcal{S}_W : \mathbb{R}^3 \times \mathbb{R} &\rightarrow \mathbb{R} & \mathcal{S}_W &= \{\mathbf{x} \in \mathbb{R}^3 : \mathcal{S}_W(\mathbf{x}, t) = 0\}; \\ \mathcal{S}_B : \mathbb{R}^3 \times \mathbb{R} &\rightarrow \mathbb{R} & \mathcal{S}_B &= \{\mathbf{x} \in \mathbb{R}^3 : \mathcal{S}_B(\mathbf{x}, t) = 0\}; \\ \mathcal{S}_L : \mathbb{R}^3 \times \mathbb{R} &\rightarrow \mathbb{R} & \mathcal{S}_L &= \{\mathbf{x} \in \mathbb{R}^3 : \mathcal{S}_L(\mathbf{x}, t) = 0\}. \end{aligned}$$

To simplify the notation, we use the same symbols to identify the subset (of \mathbb{R}^3) of the points belonging to the surface, and the function defining the surface itself.

Since all regular surfaces of \mathbb{R}^3 are locally a graph of a \mathcal{C}^∞ function, our surfaces can be described using the so called Monge parametrization: for each point $\mathbf{P} \in \mathcal{S}$ there exists a smooth function Ψ mapping points from an open set $\mathcal{A} \subseteq \mathbb{R}^2$ to $\mathcal{S} \subset \mathbb{R}^3$ such that:

$$\begin{aligned} \Psi : \mathcal{A} \subseteq \mathbb{R}^2 &\mapsto \mathbb{R}^3; \\ \mathbf{x} = (x_1, x_2) &\mapsto \mathbf{s} = (s_1(x_1, x_2), s_2(x_1, x_2), s_3(x_1, x_2)). \end{aligned}$$

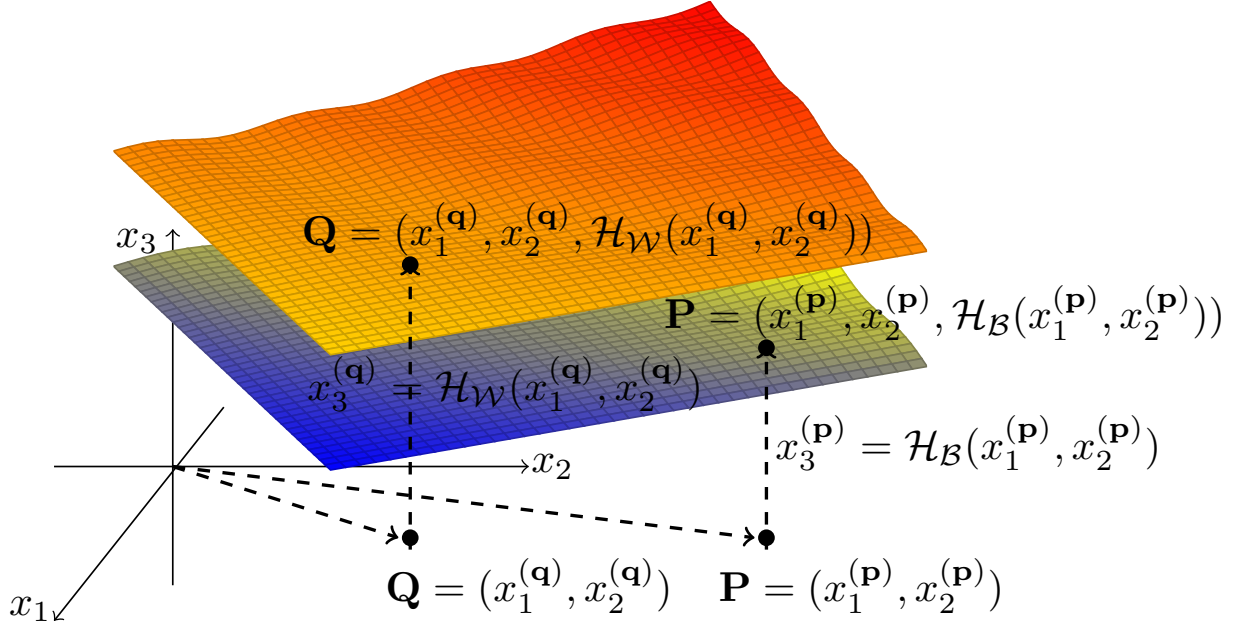


Figure 1: Example of the use of Monge parametrization to define points $\mathbf{P}_{\mathcal{H}_B}$ and $\mathbf{P}_{\mathcal{H}_W}$ on the bottom and free surfaces, respectively.

Monge parametrization is often expressed by means of a height function $\mathcal{H}(x_1, x_2)$ as:

$$\Psi : \begin{cases} s_1 = x_1, \\ s_2 = x_2, \\ s_3 = \mathcal{H}(x_1, x_2). \end{cases} \quad (2)$$

Figure 1 shows an example of the use of Monge parametrization to describe a point \mathbf{P} on the bottom surface $\mathbf{P} = (x_1^{(\mathbf{P})}, x_2^{(\mathbf{P})}, \mathcal{H}_B(x_1^{(\mathbf{P})}, x_2^{(\mathbf{P})}))$ and a point \mathbf{Q} on the free surface $\mathbf{Q} = (x_1^{(\mathbf{Q})}, x_2^{(\mathbf{Q})}, \mathcal{H}_W(x_1^{(\mathbf{Q})}, x_2^{(\mathbf{Q})}))$.

2.2. Local curvilinear coordinate system

In view of the depth integration procedure to be carried out later, we need to define a local system of curvilinear coordinates, i.e., a coordinate system spanning the fluid domain in a neighborhood $\mathcal{N}_{\mathbf{P}}$ of a point \mathbf{P} belonging to the bottom surface, and with origin in \mathbf{P} . To this end, we need a local coordinate frame, i.e., a triplet of basis vectors attached to each point $\mathbf{P} \in \mathcal{S}_B$ that can be used to describe all other points in $\mathcal{N}_{\mathbf{P}}$. This reference system will be called the ‘‘Local Curvilinear coordinate System’’ (LCS) [46].

Our construction of the LCS is based on the assumption that there exists a neighborhood $\mathcal{N}_{\mathbf{P}}$ of \mathbf{P} such that the transformation $\Phi_{\mathbf{P}}$ of each point $\mathbf{P} \in \mathcal{N}_{\mathbf{P}}$ from the global to the local coordinate is a differentiable map whose inverse is differentiable (it is a diffeomorphism). We identify these transformations as:

$$\Phi_{\mathbf{P}} : \mathbb{R}^3 \mapsto \mathbb{R}^3; \quad x_{\mathbf{P}} \mapsto s_{\mathbf{P}}, \quad \Phi_{\mathbf{P}}^{-1} : \mathbb{R}^3 \mapsto \mathbb{R}^3; \quad s_{\mathbf{P}} \mapsto x_{\mathbf{P}}, \quad (3)$$

where $x_{\mathbf{P}} = (x_1^{(\mathbf{P})}, x_2^{(\mathbf{P})}, x_3^{(\mathbf{P})})$ are the coordinates with respect to the GCS and $s_{\mathbf{P}} = (s_1^{(\mathbf{P})}, s_2^{(\mathbf{P})}, s_3^{(\mathbf{P})})$ are the corresponding coordinates with respect to the LCS. We start the actual construction by defining a reference frame for the tangent plane $\mathcal{T}_{\mathbf{P}}\mathcal{S}_B$ at every point $\mathbf{P} \in \mathcal{S}_B$ on the bottom surface, that is a pair of linearly independent vectors tangent to \mathcal{S}_B in \mathbf{P} , $(\mathbf{t}_{1,\mathbf{P}}, \mathbf{t}_{2,\mathbf{P}}) \in \mathcal{T}_{\mathbf{P}}\mathcal{S}_B$. To simplify the notation, we will often drop the subscript \mathbf{P} , but all the quantities will refer to the general point $\mathbf{P} \in \mathcal{S}_B$. The local frame is then completed by choosing the unit vector orthogonal to $\mathcal{T}_{\mathbf{P}}\mathcal{S}_B$. The two tangent vectors at \mathbf{P} can be calculated

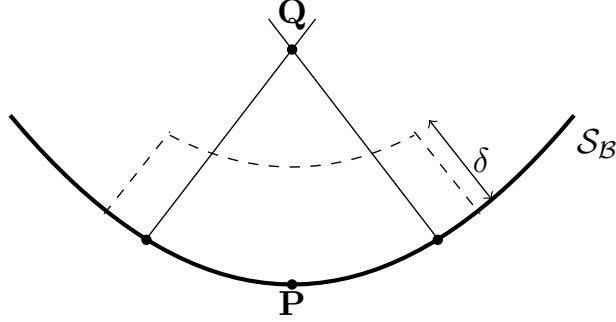


Figure 2: Example of singular point $\mathbf{Q} \in \mathcal{N}_{\mathbf{P}}$. The figure represents a vertical section of a local neighborhood $\mathcal{N}_{\mathbf{P}, \delta}$ of a parabolic point $\mathbf{P} \in \mathcal{S}_{\mathcal{B}}$.

as the differential of the transformation applied to the canonical basis of the GCS, or equivalently, as the derivatives of the transformation with respect to the local coordinates. We can write then:

$$\tilde{\mathbf{t}}_{i, \mathbf{P}} = \mathbf{d}\Phi_{\mathbf{P}}(\mathbf{e}_{i, \mathbf{P}}) = \left(\frac{\partial x_1}{\partial s_i}, \frac{\partial x_2}{\partial s_i}, \frac{\partial x_3}{\partial s_i} \right), \quad i = 1, 2,$$

where $\mathbf{d}\Phi_{\mathbf{P}}$ is the Jacobian of the coordinate transformation (3). For a regular surface, these two tangent vectors are guaranteed to exist and be linearly independent. However, since their direction depends on the curvatures of $\mathcal{S}_{\mathcal{B}}$ at \mathbf{P} , they may become approximately parallel, potentially leading to numerical ill-conditioning. For this reason, vector $\tilde{\mathbf{t}}_2$ is orthogonalized with respect to $\tilde{\mathbf{t}}_1$ via Gram-Schmidt, yielding \mathbf{t}_1 and \mathbf{t}_2 such that $\langle \mathbf{t}_1, \mathbf{t}_2 \rangle = 0$. Note that, to make sure that our LCS is properly defined, normalization of these two basis vectors cannot be done. In fact, a local orthonormal coordinate frame cannot exist as this would amount to assume a zero local Gaussian curvature of $\mathcal{S}_{\mathcal{B}}$ [44], which would imply $\mathcal{S}_{\mathcal{W}}$ parallel to $\mathcal{S}_{\mathcal{B}}$, i.e., the same assumption implicitly contained in [23] and [47]. Finally, the frame-completing vector \mathbf{t}_3 can be chosen to be unitary and orthogonal to \mathbf{t}_1 and \mathbf{t}_2 .

In the case of the Monge parametrization, indicating with subscripts partial differentiation with respect to the same variable, e.g., $\mathcal{H}_{\mathcal{B}_{s_1}} = \partial \mathcal{H}_{\mathcal{B}} / \partial s_1$, we can write explicitly the expressions for the frame vectors. After Gram-Schmidt orthogonalization and appropriate normalization, they read:

$$\begin{aligned} \mathbf{t}_{1, \mathbf{P}} &= [1; 0; \mathcal{H}_{\mathcal{B}_{s_1}}], \\ \mathbf{t}_{2, \mathbf{P}} &= \left[-\frac{\mathcal{H}_{\mathcal{B}_{s_1}} \mathcal{H}_{\mathcal{B}_{s_2}}}{1 + \mathcal{H}_{\mathcal{B}_{s_1}}^2}; 1; \frac{\mathcal{H}_{\mathcal{B}_{s_2}}}{1 + \mathcal{H}_{\mathcal{B}_{s_1}}^2} \right], \\ \mathbf{t}_{3, \mathbf{P}} = \mathbf{n}(\mathbf{P}) &= \frac{\tilde{\mathbf{t}}_{1, \mathbf{P}} \wedge \tilde{\mathbf{t}}_{2, \mathbf{P}}}{\|\tilde{\mathbf{t}}_{1, \mathbf{P}}\| \|\tilde{\mathbf{t}}_{2, \mathbf{P}}\|} = \frac{1}{\sqrt{\det(\mathcal{G}_{\mathbf{P}})}} [-\mathcal{H}_{\mathcal{B}_{s_1}}, -\mathcal{H}_{\mathcal{B}_{s_2}}, 1]. \end{aligned}$$

The first fundamental form $\mathcal{G}_{\mathbf{P}}$ of the surface at $\mathbf{P} \in \mathcal{S}_{\mathcal{B}}$, or metric tensor, is derived directly from natural \mathbb{R}^3 scalar product and is given explicitly by:

$$\mathcal{G}_{\mathbf{P}} = [g_{ij}] = \begin{bmatrix} \|\mathbf{t}_1\|^2 & 0 \\ 0 & \|\mathbf{t}_2\|^2 \end{bmatrix} = \begin{bmatrix} 1 + \mathcal{H}_{\mathcal{B}_{s_1}}^2 & 0 \\ 0 & \frac{1 + \mathcal{H}_{\mathcal{B}_{s_1}}^2 + \mathcal{H}_{\mathcal{B}_{s_2}}^2}{1 + \mathcal{H}_{\mathcal{B}_{s_1}}^2} \end{bmatrix}. \quad (4)$$

Given a neighborhood $\mathcal{N}_{\mathbf{P}}$ of \mathbf{P} , every point $\mathbf{Q} \in \mathcal{N}_{\mathbf{P}}$ can be expressed in the LCS as follows. Let $\mathbf{Q} \in \mathcal{N}_{\mathbf{P}}$ be given in the GCS by $\mathbf{Q} = (x_1^{(\mathbf{q})}, x_2^{(\mathbf{q})}, x_3^{(\mathbf{q})})$. Consider the line passing through \mathbf{Q} and parallel to $\mathbf{n}(\mathbf{P})$, which can be given the following parametric form:

$$\gamma(\lambda) : \lambda \mapsto (x_1^{(\mathbf{q})}, x_2^{(\mathbf{q})}, x_3^{(\mathbf{q})}) - \mathbf{n}(\mathbf{P})\lambda,$$

with $r = \gamma(\bar{\lambda})$ the intersection between the coordinate line γ and \mathcal{S}_B . Hence, the direct and inverse transformations of \mathbf{Q} are explicitly given by:

$$\begin{aligned}\Phi_{\mathbf{Q}} &: (s_1^{(\mathbf{q})}, s_2^{(\mathbf{q})}, s_3^{(\mathbf{q})}) := (x_1^{(r)}, x_2^{(r)}, \bar{\lambda}), \\ \Phi_{\mathbf{Q}}^{-1} &: (x_1^{(\mathbf{q})}, x_2^{(\mathbf{q})}, x_3^{(\mathbf{q})}) := \left(s_1^{(\mathbf{q})}, s_2^{(\mathbf{q})}, \mathcal{H}_B(s_1^{(\mathbf{q})}, s_2^{(\mathbf{q})}) + \mathbf{n}(\mathbf{P})s_3^{(\mathbf{q})} \right).\end{aligned}$$

The LCS thus defined is not a global bijection. In fact, singular points may arise, for example, at the intersection of normal vectors leaving \mathcal{S}_B at points belonging to $\mathcal{N}_{\mathbf{P}}$, as exemplified in figure 2 where a neighborhood of a parabolic point is shown. However, it can be proved that this LCS is a diffeomorphism in a δ -neighborhood of \mathbf{P} . In other words, there exists a positive real number δ such that, given a neighborhood of \mathbf{P} on the bottom surface, $\mathcal{A}_{\mathbf{P}} \subset \mathcal{S}_B$, we can define $\mathcal{N}_{\mathbf{P},\delta} = \mathcal{A}_{\mathbf{P}} \times [0, \delta]$ where $\Phi_{\mathbf{Q}}$ and $\Phi_{\mathbf{Q}}^{-1}$ exist for each point \mathbf{Q} in this neighborhood and are continuous, i.e., the transformation of coordinates is a diffeomorphism. Thus, the normal depth of the fluid domain must in general be smaller than δ , a condition that is satisfied if δ is chosen small enough. As exemplified in figure 2, the intuitive explanation of this condition is that the flow depth must be smaller than the minimum radius of curvature. This would be a rigorous statement when using the intrinsic coordinates, i.e., coordinates defined along geodesic (minimum length) curves on the surface. However calculation of geodesic curves is a difficult numerical and analytical task, and this is the reason why intrinsic coordinates are not used in this work. This introduces limitations on the curvature of \mathcal{S}_B at \mathbf{P} [48]. Note that if we use the exact cross-flow paths to define a curvilinear s_3 and $\mathbf{t}_{3,\mathbf{P}}$ the ensuing LCS will always be a diffeomorphism with no limitations on the curvature. Finally, it can be shown that the frame vector fields of this LCS commute, i.e., their Lie Bracket vanishes [44], a necessary and sufficient condition for the proper definition of the coordinate system [49]. This last property implies that every point on the bottom surface can be reached by following coordinate curves independently of their order.

We use the above defined LCS to express every point of $\mathcal{N}_{\mathbf{P},\delta}$ and to write the NS equations in local curvilinear coordinates. Since our intention is to depth-average these equations by integration along the normal direction and not the cross-flow paths, we can assume that the coordinate curve along s_3 is rectilinear. Hence, the expression for the elements of the diagonal three-dimensional metric tensor in $\mathcal{N}_{\mathbf{P},\delta}$ can be written as:

$$h_i = \sqrt{g_{ii}}, \quad i = 1, 2.$$

The derivatives of these functions can also be calculated explicitly, yielding the following properties of the metric tensor:

$$h_3 = 1, \quad \frac{\partial h_3}{\partial s_i} = 0, \quad i = 1, 2, 3; \quad \frac{\partial h_i}{\partial s_3} = 0, \quad i = 1, 2, 3. \quad (5)$$

The affine connection (or Christoffel symbols) of \mathcal{S}_B at \mathbf{P} can be written as:

$$\Gamma_{ij}^k = \sum_{m=1}^3 \frac{1}{2} g^{mk} \left(\frac{\partial g_{mi}}{\partial x_j} + \frac{\partial g_{mj}}{\partial x_i} - \frac{\partial g_{ij}}{\partial x_m} \right),$$

where g^{mk} are the elements of the inverse metric tensor defined in (4), so that $\sum_m g^{im} g_{mj} = \delta_{ij}$.

2.2.1. Operators in curvilinear coordinates

In this section we write out the explicit formulas for the operators needed to express the NS equation in covariant form where (5) is enforced. The covariant gradient of a scalar function f is:

$$\nabla_c f = \left(\frac{1}{h_1} \frac{\partial f}{\partial s_1}, \frac{1}{h_2} \frac{\partial f}{\partial s_2}, \frac{\partial f}{\partial s_3} \right).$$

For example, given the gravitational potential x_3 , the gravity acceleration vector can be transformed as:

$$\begin{aligned}\mathbf{g} &= -g \nabla_c x_3 = 0 \mathbf{e}_1 + 0 \mathbf{e}_2 - g \mathbf{e}_3 = -g \nabla_c x_3 \\ &= -g \frac{1}{h_1} \frac{\partial x_3}{\partial s_1} \mathbf{t}_1 - g \frac{1}{h_2} \frac{\partial x_3}{\partial s_2} \mathbf{t}_2 - g \frac{\partial x_3}{\partial s_3} \mathbf{t}_3.\end{aligned}$$

The covariant divergence of a vector $\mathbf{u} = u_1\mathbf{t}_1 + u_2\mathbf{t}_2 + u_3\mathbf{t}_3$ takes on the form:

$$\nabla_{\mathcal{C}} \cdot \mathbf{u} = \frac{1}{h_1 h_2} \left(\frac{\partial (u_1 h_2)}{\partial s_1} + \frac{\partial (u_2 h_1)}{\partial s_2} + \frac{\partial (u_3 h_1 h_2)}{\partial s_3} \right).$$

The covariant divergence $\nabla_{\mathcal{C}} \cdot \mathbb{T}$ of a tensor $\mathbb{T} = \{\tau_{ij}\}$, written in physical components, is the vector whose j -th element is given by:

$$\begin{aligned} (\nabla_{\mathcal{C}} \cdot \mathbb{T})_j &= h_j \nabla_{\mathcal{C}} \cdot \mathbb{T}_{(j)} + \frac{1}{h_1 h_j} \left(2\tau_{1j} \frac{\partial h_j}{\partial s_1} - \tau_{11} \frac{\partial h_1}{\partial s_j} \right) \\ &\quad + \frac{1}{h_2 h_j} \left(2\tau_{2j} \frac{\partial h_j}{\partial s_2} - \tau_{22} \frac{\partial h_2}{\partial s_j} \right), \end{aligned}$$

where $\nabla_{\mathcal{C}} \cdot \mathbb{T}_{(j)}$ is the covariant divergence of the vector $\mathbb{T}_{(j)} = [\tau_{j1}, \tau_{j2}, \tau_{j3}]/h_j$.

2.3. Equations of motion in the local curvilinear system

Using the previous expressions, we can write the covariant form of Navier-Stokes equations for a viscous incompressible fluid. The compact form takes the expression:

$$\frac{\partial \mathbf{u}}{\partial t} + \nabla_{\mathcal{C}} \cdot (\mathbf{u} \otimes \mathbf{u}) = -\frac{1}{\rho} \nabla_{\mathcal{C}} \cdot (p\mathbb{I} + \mathbb{T}) + \mathbf{g}, \quad (6a)$$

$$\nabla_{\mathcal{C}} \cdot \mathbf{u} = 0, \quad (6b)$$

where all the differential operators have been defined in the previous paragraph. We would like to note that, although the form of these equations is equal to the standard compact form of the NS equations (1), the subscript in the gradient symbol $\nabla_{\mathcal{C}}$ indicates that they are written in the LCS and contain the information (metric) of the bottom surface. These equations are used to perform the depth integration over s_3 , i.e., along the direction normal to the bed, using as integration limits the bottom topography and the water surface.

3. Integration along the normal depth

For each point $\mathbf{P} \in \mathcal{S}_{\mathcal{B}}$, depth integration of the NS equations (6) is carried out along the normal direction s_3 . To this aim, we identify the bottom and the fluid free surfaces as:

$$\begin{aligned} \mathcal{S}_{\mathcal{B}}(s_1, s_2, s_3) &= \{(s_1, s_2, s_3) \in \mathbb{R}^3 : s_3 = \mathcal{H}_{\mathcal{B}}(s_1, s_2) = 0\}, \\ \mathcal{S}_{\mathcal{W}}(s_1, s_2, s_3, t) &= \{(s_1, s_2, s_3) \in \mathbb{R}^3 : \\ &\quad s_3 = \mathcal{H}_{\mathcal{W}}(s_1, s_2, t) = \eta(s_1, s_2, t) \text{ for each } t \in [0, T]\}, \end{aligned}$$

where $\eta(s_1, s_2, t) = \mathcal{H}_{\mathcal{W}}(s_1, s_2, t) - \mathcal{H}_{\mathcal{B}}(s_1, s_2)$ identifies the fluid depth (figure 3, left panel). Note that we assume that the bottom is not eroding and thus maintains a fixed geometry, while the fluid surface is a function of time. For this reason, we have included the time-dependence in the functional forms of both $\mathcal{S}_{\mathcal{W}}$ and η but not in $\mathcal{S}_{\mathcal{B}}$. The kinematic condition at the fluid-air boundary postulates that the free surface is a material interface that moves with the fluid. The bottom boundary is assumed to be impermeable. Thus we have:

$$\frac{d\mathcal{S}_{\mathcal{W}}}{dt} = \frac{\partial \mathcal{S}_{\mathcal{W}}}{\partial t} + \mathbf{u}_{\mathcal{H}_{\mathcal{W}}} \cdot \nabla \mathcal{S}_{\mathcal{W}} = 0, \quad s_3 = \eta, \quad (7)$$

$$\frac{d\mathcal{S}_{\mathcal{B}}}{dt} = \mathbf{u}_{\mathcal{H}_{\mathcal{B}}} \cdot \nabla \mathcal{S}_{\mathcal{B}} = 0, \quad s_3 = 0; \quad (8)$$

where the surface velocities coincide with the three-dimensional fluid velocity, i.e., $\mathbf{u}_{\mathcal{H}_{\mathcal{B}}} = \mathbf{u}|_{\mathcal{H}_{\mathcal{B}}}$ and $\mathbf{u}_{\mathcal{H}_{\mathcal{W}}} = \mathbf{u}|_{\mathcal{H}_{\mathcal{W}}}$. Using the definition of $\mathcal{S}_{\mathcal{W}}$ and η , we have immediately:

$$\frac{\partial \eta}{\partial t} + \mathbf{u} \cdot \nabla_{\mathcal{C}} \eta = 0, \quad s_3 = \eta. \quad (9)$$

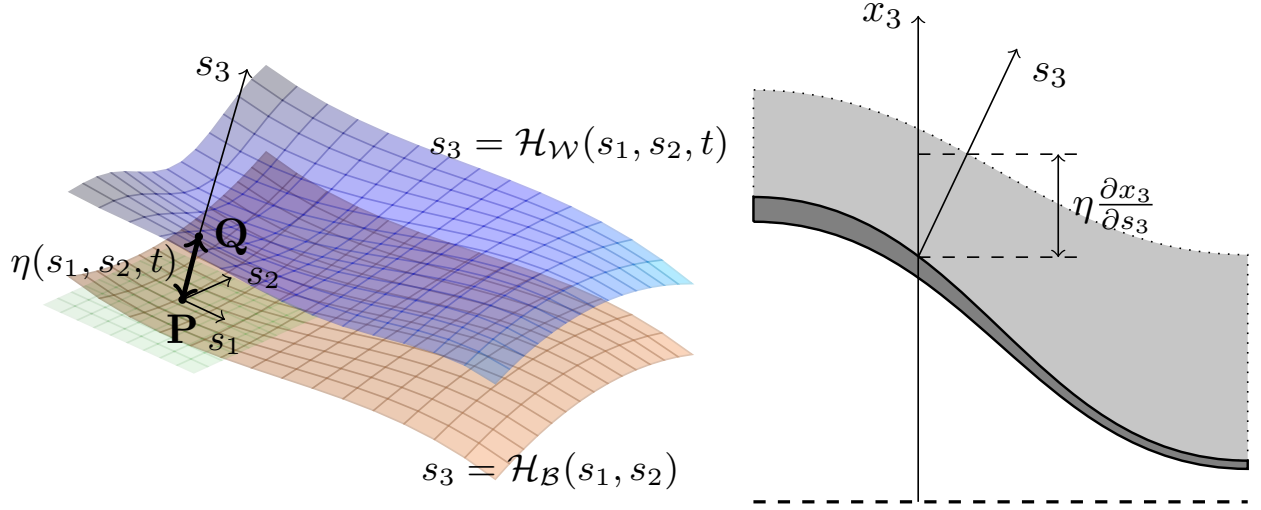


Figure 3: Definition of the water depth $\eta(s_1, s_2, t)$ on the local Monge patch at point $\mathbf{P} \in \mathcal{S}_B$ as the distance between \mathcal{S}_B and \mathcal{S}_W evaluated along the normal direction starting from \mathbf{P} (left panel). Pressure distribution along the normal direction s_3 (right panel).

Assuming that external actions on the free surface are negligible, the dynamic condition at the fluid-air interface translates into a zero-stress boundary equation:

$$\mathbb{T}_{\mathcal{H}_W} \cdot \mathbf{n}_{\mathcal{H}_W} = 0, \quad \mathbf{n}_{\mathcal{H}_W} = \frac{\nabla \mathcal{H}_W}{\|\nabla \mathcal{H}_W\|} \quad (10)$$

where $\mathbf{n}_{\mathcal{H}_W}$ is the normal vector to the free water surface \mathcal{H}_W . The bed boundary condition imposes the value of the shear stress:

$$\mathbb{T}_{\mathcal{H}_B} \cdot \mathbf{n} = \mathbf{f}_{\mathcal{H}_B} = p_{\mathcal{H}_B} \mathbf{n} + \tau_{b_1} \mathbf{t}_1 + \tau_{b_2} \mathbf{t}_2, \quad (11)$$

where $p_{\mathcal{H}_B}$ is the pressure at the bed surface and τ_{b_i} denotes bottom friction stresses.

The velocity vector is split into a depth average value, $\bar{\mathbf{u}}$, plus a departure from the average, $\tilde{\mathbf{u}}$:

$$\mathbf{u} = \bar{\mathbf{u}} + \tilde{\mathbf{u}}, \quad \bar{\mathbf{u}}(s_1, s_2, t) = \frac{1}{\eta} \int_0^\eta \mathbf{u}(\mathbf{s}, t) \, ds_3, \quad \int_0^\eta \tilde{\mathbf{u}}(\mathbf{s}, t) \, ds_3 = 0. \quad (12)$$

We will often use the following relationship derived directly from Leibnitz rule:

$$\int_0^\eta \frac{\partial u_i(\mathbf{s}, t)}{\partial t} \, ds_3 = \frac{\partial}{\partial t} \left(\int_0^\eta u_i(\mathbf{s}, t) \, ds_3 \right) - \left[u_i \frac{\partial \mathcal{H}_W}{\partial t} \right]_{s_3=\eta} = \frac{\partial \eta \bar{u}_i}{\partial t} - \left[u_i \frac{\partial \mathcal{H}_W}{\partial t} \right]_{s_3=\eta}. \quad (13)$$

Depth integration starts with the mass continuity equation (6b). We have:

$$\int_0^\eta \left[\frac{\partial (u_1 h_2)}{\partial s_1} + \frac{\partial (u_2 h_1)}{\partial s_2} + \frac{\partial (u_3 h_1 h_2)}{\partial s_3} \right] \, ds_3 = 0.$$

Application of Leibnitz Rule (13) yields:

$$\frac{\partial}{\partial s_1} \int_0^\eta u_1 h_2 \, ds_3 + \frac{\partial}{\partial s_2} \int_0^\eta u_2 h_1 \, ds_3 - [\mathbf{u} \cdot \nabla_c \eta]_{s_3=\eta} = 0.$$

From the definition of the average velocity $\bar{\mathbf{u}}$, using eq. (9) we obtain:

$$\begin{aligned}\int_0^\eta u_i h_j \, ds_3 &= \int_0^\eta (\bar{u}_i + \tilde{u}_i) h_j \, ds_3 \\ &= \bar{u}_i h_j \int_0^\eta ds_3 + h_j \int_0^\eta \tilde{u}_i \, ds_3 = \eta \bar{u}_i h_j, \quad i, j = 1, 2.\end{aligned}$$

where we have used the fact that h_j does not depend on s_3 . Setting $q_i = \eta \bar{u}_i$ and using the chain rule we finally obtain:

$$\begin{aligned}\frac{\partial \eta}{\partial t} + \frac{\partial}{\partial s_1} \left(\frac{q_1}{h_1} \right) + \frac{\partial}{\partial s_2} \left(\frac{q_2}{h_2} \right) \\ + \left(\frac{1}{h_2} \frac{\partial h_2}{\partial s_1} + \frac{1}{h_1} \frac{\partial h_1}{\partial s_1} \right) \frac{q_1}{h_1} + \left(\frac{1}{h_2} \frac{\partial h_2}{\partial s_2} + \frac{1}{h_1} \frac{\partial h_1}{\partial s_2} \right) \frac{q_2}{h_2} = 0,\end{aligned}$$

Note that the use of Leibnitz theorem and the related chain rule of differentiation implicitly assumes continuity of the solution and its derivatives (both water depth η and velocity \mathbf{u}) thus in principle ruling out the formation of shocks. Only recently, theoretical studies on the use of the chain rule for BV (Bounded Variation) functions have been proposed [50, 51], but their practical applications in numerical solvers seems to be still far reaching.

Now we turn our attention to the third (s_3) equation of (6a). It is worthwhile writing this equation on a fully curvilinear system (i.e., s_3 is curvilinear and not straight as in our LCS) so that the effects of following the cross-flow are rendered explicitly:

$$\begin{aligned}\frac{\partial u_3}{\partial t} + \frac{1}{h_1 h_2 h_3} \left(\frac{\partial (u_1 u_3 h_2 h_3)}{\partial s_1} + \frac{\partial (u_2 u_3 h_1 h_3)}{\partial s_2} + \frac{\partial (u_3^2 h_1 h_2)}{\partial s_3} \right) \\ - \frac{u_1^2}{h_1 h_3} \frac{\partial h_1}{\partial s_3} + \frac{u_1 u_3}{h_1 h_3} \frac{\partial h_3}{\partial s_1} - \frac{u_2^2}{h_2 h_3} \frac{\partial h_2}{\partial s_3} + \frac{u_2 u_3}{h_2 h_3} \frac{\partial h_3}{\partial s_2} = \\ = - \frac{1}{\rho} \frac{1}{h_3} \frac{\partial p}{\partial s_3} - \frac{1}{h_3} \frac{\partial x_3}{\partial s_3} g - \frac{1}{\rho} \frac{1}{h_1 h_2 h_3} \left(\frac{\partial (\tau_{31} h_2 h_3)}{\partial s_1} \right. \\ \left. + \frac{\partial (\tau_{32} h_1 h_3)}{\partial s_2} + \frac{\partial (\tau_{33} h_1 h_2)}{\partial s_3} \right) \\ \left. + \frac{1}{\rho} \left(\frac{\tau_{11}}{h_1 h_3} \frac{\partial h_1}{\partial s_3} - \frac{\tau_{13}}{h_1 h_3} \frac{\partial h_3}{\partial s_1} + \frac{\tau_{22}}{h_2 h_3} \frac{\partial h_2}{\partial s_3} - \frac{\tau_{23}}{h_2 h_3} \frac{\partial h_3}{\partial s_2} \right).\end{aligned}$$

Note the presence of terms containing h_j and its derivatives. In the case of a fully curvilinear LCS these terms may be important, depending on the curvatures of the cross-flow. In our case they are zero because of (5). The SW approximation in our curvilinear system is equivalent to assume that the s_3 -component of the velocity is negligible. Hence, in the previous equation we drop all the terms that contain u_3 , including $\tau_{3i} = \tau_{i3}$, $i = 1, 2, 3$, to obtain:

$$\int_0^\eta \frac{1}{\rho} \frac{\partial p}{\partial s_3} \, ds_3 + \int_0^\eta \frac{\partial x_3}{\partial s_3} g \, ds_3 \approx 0,$$

which states that the pressure varies proportionally to $\partial x_3 / \partial s_3$ along the direction normal to the bed. Note that if we followed the cross-flow paths during depth integration, since along these surface $u_3 = 0$, the above equation would be exact, but with extra terms involving h_3 and $\partial h_3 / \partial s_i$. The expression for the pressure at the bottom surface then reads (see figure 3, right panel):

$$p_{\mathcal{H}_B} = \rho g \eta \frac{\partial x_3}{\partial s_3}. \quad (14)$$

This expression will be used during depth-integration of the s_1 and s_2 momentum conservation equations to evaluate the pressure terms as a function of the depth η . We would like to remark that $x_3 = x_3(s_1, s_2, s_3)$

and its derivative are evaluated through the scalar product:

$$\frac{\partial x_3}{\partial s_3} = \frac{\mathbf{e}_3 \cdot \mathbf{n}}{\|\mathbf{e}_3\| \|\mathbf{n}\|} = \frac{1}{\sqrt{1 + \mathcal{H}_{\mathcal{B}_{s_1}}^2 + \mathcal{H}_{\mathcal{B}_{s_2}}^2}}.$$

Next, we focus on the s_1 -momentum conservation equation. Applying depth-integration, using Leibnitz rule together with the kinematic equations (9) and (8), and the dynamic conditions (10) and (11), and incorporating the hydrostatic pressure condition (14), we obtain:

$$\begin{aligned} & \frac{\partial q_1}{\partial t} + \frac{\partial}{\partial s_1} \left(\frac{\alpha_{11} q_1^2}{h_1 \eta} + g \frac{\eta^2}{2h_1} \frac{\partial x_3}{\partial s_3} \right) + \frac{\partial}{\partial s_2} \left(\frac{\alpha_{12} q_1 q_2}{h_2 \eta} \right) \\ & + \left(\frac{1}{h_1} \frac{\partial h_1}{\partial s_1} + \frac{1}{h_2} \frac{\partial h_2}{\partial s_1} \right) \frac{\alpha_{11} q_1^2}{h_1 \eta} \\ & + \left(\frac{2}{h_1} \frac{\partial h_1}{\partial s_2} + \frac{1}{h_2} \frac{\partial h_2}{\partial s_2} \right) \frac{\alpha_{12} q_1 q_2}{h_2 \eta} - \left(\frac{1}{h_1} \frac{\partial h_2}{\partial s_1} \right) \frac{\alpha_{22} q_2^2}{h_2 \eta} \\ & = -g\eta \frac{1}{h_1} \frac{\partial x_3}{\partial s_1} - \frac{1}{2h_1} g\eta^2 \frac{\partial}{\partial s_1} \left(\frac{\partial x_3}{\partial s_3} \right) - \frac{1}{2h_1^2} g\eta^2 \frac{\partial h_1}{\partial s_1} \frac{\partial x_3}{\partial s_3} - \frac{1}{\rho} \mathbb{T}_{\mathcal{H}_{\mathcal{B},1}} \cdot \mathbf{n} \\ & - \frac{1}{\rho} \left[\frac{\partial}{\partial s_1} \left(\frac{1}{h_1} \int_0^\eta \tau_{11} ds_3 \right) + \frac{\partial}{\partial s_2} \left(\frac{1}{h_2} \int_0^\eta \tau_{12} ds_3 \right) \right. \\ & + \left(\frac{1}{h_1} \frac{\partial h_1}{\partial s_1} + \frac{1}{h_2} \frac{\partial h_2}{\partial s_1} \right) \frac{1}{h_1} \int_0^\eta \tau_{11} ds_3 \\ & + \left(\frac{2}{h_1} \frac{\partial h_1}{\partial s_2} + \frac{1}{h_2} \frac{\partial h_2}{\partial s_2} \right) \frac{1}{h_2} \int_0^\eta \tau_{12} ds_3 \\ & \left. - \frac{1}{h_1} \frac{\partial h_2}{\partial s_1} \frac{1}{h_2} \int_0^\eta \tau_{22} ds_3 \right], \end{aligned}$$

where:

$$\alpha_{ij} = \frac{1}{\eta} \int_0^\eta \left(1 + \frac{\tilde{u}_i \tilde{u}_j}{\bar{u}_i \bar{u}_j} \right) ds_3$$

with obvious analogue for the s_2 counterpart. The coefficients α_{ij} incorporate deviations from the the average of the velocity profile along the local normal direction. Effectively, they can be considered as a contribution to the lateral momentum exchanges and thus added to the stresses τ_{ij} (e.g., viscous and turbulent). Taking origin from the decomposition (12), these terms are often called differential advection terms [32], or, considering their stress-like nature, as residual dispersive stresses [33–35]. In principle, their evaluation requires the knowledge of the fully three-dimensional structure of the flow field. However, unlike typical turbulent and viscous stresses, they cannot be modeled by a simple diffusive approach [32]. In some special cases, quasi-three dimensional models have then been used to model their effects [3, 52, 53]. More often, they are disregarded in conventional two-dimensional models of geophysical flows [36] and even in Boussinesq-type models that assumes a depth-varying turbulence averaged velocity [34]. For these reasons, as a first approximation we neglect these terms as well as the depth averaged contributions of τ_{ij} , thus effectively incorporating their effects into the uncertainty of the empirical friction coefficients.

In summary, the final covariant form of the SWE written in the local orthogonal curvilinear coordinate

system for $\alpha_{ij} = 1$ is given by:

$$\frac{\partial \eta}{\partial t} + \frac{\partial}{\partial s_1} \left(\frac{q_1}{h_1} \right) + \frac{\partial}{\partial s_2} \left(\frac{q_2}{h_2} \right) + S_1^M = 0, \quad (15a)$$

$$\frac{\partial q_1}{\partial t} + \frac{\partial}{\partial s_1} \left(\frac{1}{h_1} \frac{q_1^2}{\eta} + g \frac{\eta^2}{2h_1} \frac{\partial x_3}{\partial s_3} \right) + \frac{\partial}{\partial s_2} \left(\frac{1}{h_2} \frac{q_1 q_2}{\eta} \right) + S_2^F + S_2^M = 0, \quad (15b)$$

$$\frac{\partial q_2}{\partial t} + \frac{\partial}{\partial s_1} \left(\frac{1}{h_1} \frac{q_1 q_2}{\eta} \right) + \frac{\partial}{\partial s_2} \left(\frac{1}{h_2} \frac{q_2^2}{\eta} + g \frac{\eta^2}{2h_2} \frac{\partial x_3}{\partial s_3} \right) + S_3^F + S_3^M = 0. \quad (15c)$$

The terms S_k^F and S_k^M are the k -th components of the vectors containing gravity and friction forces, and derivatives of the metric coefficients, as expressed by:

$$\mathbf{S}^F = \begin{bmatrix} 0 \\ \tau_{b_1} + g \frac{\eta}{h_1} \frac{\partial x_3}{\partial s_1} \\ \tau_{b_2} + g \frac{\eta}{h_2} \frac{\partial x_3}{\partial s_2} \end{bmatrix}$$

and

$$\mathbf{S}^M = \begin{bmatrix} \left(\frac{1}{h_2} \frac{\partial h_2}{\partial s_1} + \frac{1}{h_1} \frac{\partial h_1}{\partial s_1} \right) \frac{q_1}{h_1} + \left(\frac{1}{h_2} \frac{\partial h_2}{\partial s_2} + \frac{1}{h_1} \frac{\partial h_1}{\partial s_2} \right) \frac{q_2}{h_2} \\ \frac{\partial h_1}{\partial s_1} \frac{1}{h_1^2} \left(\frac{q_1^2}{\eta} + g \frac{\eta^2}{2} \frac{\partial x_3}{\partial s_3} \right) + \frac{\partial h_1}{\partial s_2} \frac{2}{h_1 h_2} \frac{q_1 q_2}{\eta} + \frac{\partial h_2}{\partial s_1} \frac{1}{h_1 h_2} \left(\frac{q_1^2}{\eta} - \frac{q_2^2}{\eta} \right) \\ + \frac{\partial h_2}{\partial s_2} \frac{1}{h_2^2} \frac{q_1 q_2}{\eta} + g \frac{\eta^2}{2h_1} \frac{\partial}{\partial s_1} \left(\frac{\partial x_3}{\partial s_3} \right) \\ \frac{\partial h_1}{\partial s_1} \frac{1}{h_1^2} \frac{q_1 q_2}{\eta} + \frac{\partial h_1}{\partial s_2} \frac{1}{h_1 h_2} \left(\frac{q_2^2}{\eta} - \frac{q_1^2}{\eta} \right) + \frac{\partial h_2}{\partial s_1} \frac{2}{h_1 h_2} \frac{q_1 q_2}{\eta} \\ + \frac{\partial h_2}{\partial s_2} \frac{1}{h_2^2} \left(\frac{q_2^2}{\eta} + g \frac{\eta^2}{2} \frac{\partial x_3}{\partial s_3} \right) + g \frac{\eta^2}{2h_2} \frac{\partial}{\partial s_2} \left(\frac{\partial x_3}{\partial s_3} \right). \end{bmatrix}$$

Equation (15) is finally written in vector form as:

$$\frac{\partial \mathbf{U}}{\partial t} + \nabla \cdot \underline{\underline{F}} + \mathbf{S} = 0, \quad (16)$$

where

$$\mathbf{U} = \begin{bmatrix} \eta \\ q_1 \\ q_2 \end{bmatrix}, \quad \underline{\underline{F}} = \begin{bmatrix} \frac{q_1}{h_1} & \frac{q_2}{h_2} \\ \frac{1}{h_1} \frac{q_1^2}{\eta} + g \frac{\eta^2}{2h_1} \frac{\partial x_3}{\partial s_3} & \frac{1}{h_2} \frac{q_1 q_2}{\eta} \\ \frac{1}{h_1} \frac{q_1 q_2}{\eta} & \frac{1}{h_2} \frac{q_2^2}{\eta} + g \frac{\eta^2}{2h_2} \frac{\partial x_3}{\partial s_3} \end{bmatrix}, \quad \mathbf{S} = \mathbf{S}^F + \mathbf{S}^M.$$

4. The Numerical Model

The numerical solution of equation (16) is obtained by means of a Finite Volume (FV) scheme based on a first order accurate Godunov method [54] combined with a centered flux approximation as provided by the FORCE scheme [55]. The reason for the choice of a low order discretization is that we want to highlight the importance of the correct geometrical formulation of the SWE system rather than focus on their numerical discretization. Thus, we adopt a simple but robust solver, favoring resiliency over accuracy. In fact, robustness and accuracy seldom coexist and higher order schemes often lead to erroneous results

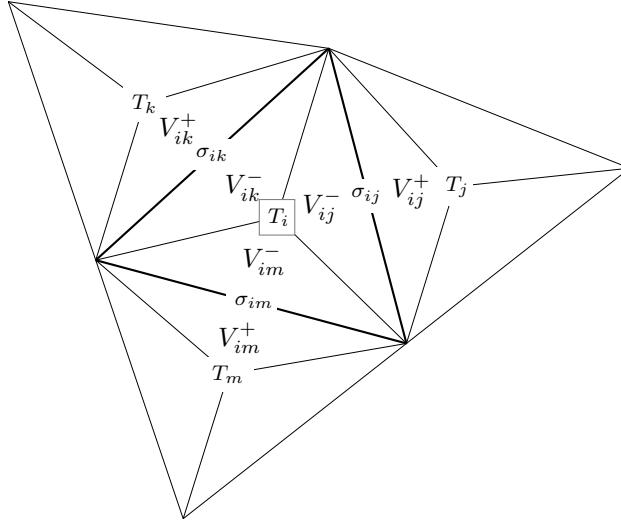


Figure 4: Notation for a general configuration on an unstructured triangular mesh.

(see e.g. [56]) because of potential ill-conditioning intrinsic to the discretization method [57]. Hence, we adopt a robust central-upwind Godunov-type scheme as proposed by [58, 59]. The numerical fluxes are evaluated using the FORCE approximation that does not require ad-hoc Riemann solvers [55]. In our case of non-autonomous fluxes, a precise definition of the Riemann problem is not available. A few attempts have been proposed in the literature [28, 60], but more work along this direction is needed. The use of such an approach would introduce uncontrolled errors in the wave speeds and characteristic curves. Hence we decided to use a "non-geometric" solver based on a central flux approximation that does not require the definition of a Riemann problem.

Application of the FV method requires the discretization of the bottom surface. For the reasons stated above, i.e., to focus exclusively on the geometrical characteristics of the proposed SW equations, we decide to define the bottom topography with a known analytical function, so that arc lengths, surface areas, and integrals on the FV cells can be evaluated as accurately as possible. This is achieved by first triangulating the planar domain formed by the union of the two-dimensional Monge patches $\bigcup \mathcal{A} \subset \mathbb{R}^2$ (i.e., the projection of the bottom surface on the (x_1, x_2) coordinate plane) and then raising the vertical coordinate of the resulting mesh nodes using the Monge function. Thus, the global coordinates of mesh node i on the bottom surface are given by $(x_1^{(i)}, x_2^{(i)}, \mathcal{H}_B(x_1^{(i)}, x_2^{(i)}))$. Potentially badly shaped surface triangles are corrected a posteriori by manual intervention or by local mesh refinement. The relevant geometrical characteristics, such as metric coefficients, are defined analytically on each triangle, which is thus identified with the local Monge patch. For practical applications, the description of bottom topography is generally based on observed data and the above procedure no longer applies. Starting from a measured DEM (Digital Elevation Model), metric coefficients will need to be evaluated numerically, with consequential loss of accuracy. The issue of bottom surface definition from observations and the numerical approximation of the needed geometrical quantities is beyond the purpose of the current paper and will be addressed in future work. For the same reason, problems related to well-balance and fluid-at-rest, as well as wetting-and-drying algorithms are not addressed specifically.

4.1. Description of the surface triangulation

Let the domain be discretized by a surface triangulation \mathcal{T}_ℓ , which is assumed to be regular and identified by the maximum arc length ℓ . The domain of definition of (16) Ω is assumed to be a polygonally shaped closed subset of \mathcal{H}_B and is formed by the union of non-intersecting triangular cells ($\Omega = \mathcal{T}_\ell = \bigcup_i T_i$). We denote the surface area of T_i with the symbol $|T_i|$, while σ_{ij} represents the edge between cell T_i and T_j , $\sigma_{ij} = T_i \cap T_j$, whose arc length is given by $|\sigma_{ij}|$. The unit normal vector is indicated with \mathbf{n}_{ij} and is directed

from T_i towards T_j (see figure 4). This process is adopted as it ensures that discrete values of the metric coefficients converge to the continuous counterparts when the mesh is refined. This convergence may not be warranted for meshes made up of quadrilateral or triangular elements with center of gravity defined on the surface [61].

The computation of $|T_i|$ and of $|\sigma_{ij}|$ are performed exploiting the functional form of the surface itself defined through the LCS. Accordingly, we have

$$|T_i| = \int_{T_i} h_1(s_1, s_2) h_2(s_1, s_2) \, ds_1 \, ds_2.$$

The integral above is computed using a 7-point Gaussian quadrature rule. The edge arc length is approximated as follows. Define the curve that connects the edge nodes \mathbf{P}_α and \mathbf{P}_β in parametric form as:

$$\sigma(\lambda) = \begin{cases} s_1(\lambda) = \left(s_1^{(\alpha)} - s_1^{(\beta)} \right) \lambda + s_1^{(\alpha)}, \\ s_2(\lambda) = \left(s_2^{(\alpha)} - s_2^{(\beta)} \right) \lambda + s_2^{(\alpha)}, \\ s_3(\lambda) = \mathcal{H}_B(s_1(\lambda), s_2(\lambda)), \end{cases} \quad (17)$$

where \mathbf{P}_α and \mathbf{P}_β are the two limit points of the arc, s_1 and s_2 are curvilinear coordinates written as function of a parameter λ , and s_3 is given by Monge parametrization (2). The arc length of each edge is thus the integral of curve (17):

$$\begin{aligned} |\sigma| &= \int_{\mathbf{P}_\alpha}^{\mathbf{P}_\beta} d\sigma \\ &= \int_0^1 \left(\left(s_1^{(\alpha)} - s_1^{(\beta)} \right)^2 + \left(s_2^{(\alpha)} - s_2^{(\beta)} \right)^2 + \right. \\ &\quad \left. \left(\frac{\partial \mathcal{H}_B(\lambda)}{\partial s_1} \left(s_1^{(\alpha)} - s_1^{(\beta)} \right) + \frac{\partial \mathcal{H}_B(\lambda)}{\partial s_2} \left(s_2^{(\alpha)} - s_2^{(\beta)} \right) \right)^2 \right)^{\frac{1}{2}} d\lambda, \end{aligned}$$

where we have written for simplicity $\mathcal{H}_B(\lambda) = \mathcal{H}_B(s_1(\lambda), s_2(\lambda))$. This integral is evaluated numerically by means of a 2-point Gaussian quadrature rule.

4.2. The finite volume scheme

Integrating eq. (16) over Ω , using the fact that $\int_\Omega = \sum_{i=1}^N \int_{T_i}$, exchanging the time-derivative with the integral sign, and applying Gauss' Divergence Theorem we obtain:

$$\frac{\partial}{\partial t} \int_T \mathbf{U} = - \int_{\partial T} \underline{\underline{F}} \cdot \mathbf{n} + \int_T \mathbf{S}, \quad \forall T \in \mathcal{T}_\ell.$$

Following Godunov's approach, we define the cell-averaged quantities over the triangulated surface as:

$$\mathbf{U}_i = \frac{1}{|T_i|} \int_{T_i} \mathbf{U}; \quad \mathbf{S}_i = \frac{1}{|T_i|} \int_{T_i} \mathbf{S},$$

and the edge-averaged numerical flux as:

$$\mathbf{F}_{ij} = \frac{1}{|\sigma_{ij}|} \int_{\sigma_{ij}} \underline{\underline{F}} \cdot \mathbf{n} = \langle \underline{\underline{F}}, \mathbf{n}_{ij} \rangle_{\sigma_{ij}}.$$

Using a time-splitting approach to handle the source term together with a forward Euler time-discretization, we obtain:

$$\begin{aligned} \tilde{\mathbf{U}}_i^{k+1} &= \mathbf{U}_i^k - \frac{\Delta t}{|T_i|} \sum_{j=1}^{N_s} |\sigma_{ij}| \mathbf{F}_{ij}^{FORCE}, \\ \mathbf{U}_i^{k+1} &= \tilde{\mathbf{U}}_i^{k+1} - \Delta t \mathbf{S}(\tilde{\mathbf{U}}_i^{k+1}), \end{aligned}$$

where the *FORCE* flux is defined as the average of the Lax-Friedrichs and the Lax-Wendroff fluxes:

$$\mathbf{F}_{ij}^{FORCE} = \frac{1}{2} (\mathbf{F}_{ij}^{LF} + \mathbf{F}_{ij}^{LW})$$

and these fluxes adapted to two-dimensional triangulations are given by [55]:

$$\mathbf{F}_{ij}^{LF} = \frac{V_j^- \mathbf{F}_{ij}(\mathbf{U}_j^k) + V_j^+ \mathbf{F}_{ij}(\mathbf{U}_i^k)}{V_j^- + V_j^+} - \frac{V_j^- V_j^+}{V_j^- + V_j^+} \frac{2}{\Delta t |\sigma_{ij}|} (\mathbf{U}_j^k - \mathbf{U}_i^k),$$

and

$$\mathbf{F}_{ij}^{LW} = \frac{V_j^+ \mathbf{F}_{ij}(\mathbf{U}_j^k) + V_j^- \mathbf{F}_{ij}(\mathbf{U}_i^k)}{V_j^- + V_j^+} - \frac{1}{2} \frac{|\sigma_{ij}| \Delta t}{V_j^- + V_j^+} \hat{A}_{ij} (\mathbf{F}_{ij}(\mathbf{U}_j^k) - \mathbf{F}_{ij}(\mathbf{U}_i^k)).$$

In the above equations we have used the symbols V_j^+ and V_j^- to indicate the one-sided diamond cells (see figure 4), while matrix \hat{A}_{ij} is the Jacobian of the flux matrix [41, 62]. The fluxes are evaluated at edge midpoints using the exact metric tensor (4) of the surface, and the integrals of the source terms are evaluated using the midpoint rule with exact surface triangular area.

Finally, in order to ensure the stability of the scheme, the standard CFL (Courant-Friedrichs-Lewy) condition must be satisfied. Note that the wetting-and-drying algorithm presented in [42] has been implemented in the current version of the model but has not been specifically adapted for the actual covariant form of the SWE. Thus we expect potential oscillatory behavior ahead of wave fronts. For this reason, in this first step of our research, we will design testing examples that consider only bed drying, thus avoiding the difficulties connected with wetting and drying processes.

4.3. Parallel transport

The above FV formulation requires the evaluation of differences between flux and velocity vectors calculated at the cell interfaces. Since these vectors are defined on each cell, and since each cell lies on a different tangent plane, these differences must be performed after parallel transport of the vector quantities, given the relevant parametrization. Parallel transport of a vector $\mathbf{u} \in \mathcal{H}_{\mathcal{B}}$ is obtained as the solution of the following system of ordinary differential equations defined on the surface curve connecting geodetically the gravity centers of two adjacent cells:

$$\nabla u_i \cdot \frac{d\mathbf{c}}{d\lambda} + \mathbf{u} \cdot \{\Gamma_{kl}^i\} \frac{d\mathbf{c}}{d\lambda} = 0, \quad (18)$$

where $\mathbf{c}(\lambda)$ is the parametric expression of the geodesic curve joining the two gravity centers and $\{\Gamma_{kl}^i\}$ is the matrix of the i -th Christoffel symbol. We implement parallel transport following the same simplifications made by [27]. Thus, the ODE system (18) is solved numerically using a first order explicit Euler method along the curve parameter λ . Given two triangles T_i and T_j adjacent through edge σ_{ij} , we denote with s_i the LCS coordinates of the gravity center of T_i and with s_{ij} the LCS coordinates of the midpoint of σ_{ij} . The index (subscript or superscript) (i) relates quantities calculated on cell T_i using the related LCS. We also assume that the geodesic curve is always along the s_1 direction, which is then assumed to coincide with the direction of the principal curvature. With all these assumptions, a generic vector $\mathbf{u} \in \mathcal{H}_{\mathcal{B}}$ is parallel transported using the following formulas:

$$\begin{aligned} u_1^{(i)}(s_{ij}) &= u_1(s_i) - (s_{1,ij} - s_{1,i}) \left(\Gamma_{11}^{1,(i)} u_1(s_i) + \Gamma_{21}^{1,(i)} u_2(s_i) \right), \\ u_2^{(i)}(s_{ij}) &= u_2(s_i) - (s_{1,ij} - s_{1,i}) \left(\Gamma_{11}^{2,(i)} u_1(s_i) + \Gamma_{21}^{2,(i)} u_2(s_i) \right), \\ u_1^{(j)}(s_{ij}) &= u_1(s_j) - (s_{1,ij} - s_{1,j}) \left(\Gamma_{11}^{1,(j)} u_1(s_j) + \Gamma_{21}^{1,(j)} u_2(s_j) \right), \\ u_2^{(j)}(s_{ij}) &= u_2(s_j) - (s_{1,ij} - s_{1,j}) \left(\Gamma_{11}^{2,(j)} u_1(s_j) + \Gamma_{21}^{2,(j)} u_2(s_j) \right). \end{aligned}$$

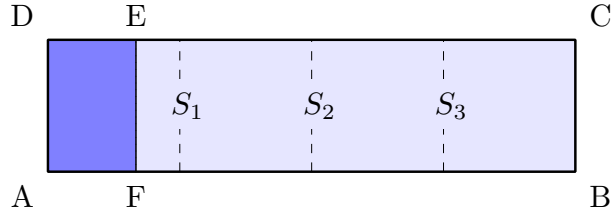


Figure 5: Sketch of the two-dimensional Monge patch $\mathcal{A} \subset \mathbb{R}^2$ defining the domain of all the test cases. The water depth initial conditions are shown in blue shades (dark identifies deeper upstream depth) together with the location of the three cross-sections where discharges are evaluated.

5. Simulations and Numerical Results

The present section describes three synthetic test cases designed to analyze the influence of the bottom geometry (slope and curvature) on the solution of the SWE. The design needs to be aware of the assumptions leading to our formulation, and most importantly of the hypothesis of slowly varying topography with small curvatures. Moreover, we want to minimize the influence of critical, but not relevant to geometrical effects, numerical algorithms, such as wetting-drying treatment or water-at-rest enforcement. At the same time boundary and initial conditions should have minimal effects on the accuracy of the numerical solution.

Our experiments must then have always a nonzero downstream water depth to avoid wetting phenomena. Moreover, the fluid velocity must always be large enough so that well-balance errors are negligible. Then we are forced to use initial conditions that are in non-equilibrium states, a situation that is difficult to reproduce in laboratory experiments. Moreover, there are no explicit solutions of our mathematical model and thus we cannot evaluate discretization errors. As a consequence, the only possible and significative comparison is versus the solution of the same model without geometric information, i.e., setting $h_i = 1$.

To achieve these goals the domain is defined via Monge parametrization starting from a regular triangulation of a rectangular subset $\mathcal{A} \subset \mathbb{R}^2$ (Figure 5) and using a sufficiently smooth height function. All the test cases implement a simulation where a gravity wave moves downward starting with initial conditions involving water depths that are sufficiently large to minimize the drying of the bottom and exclude re-wetting. We avoid topographies with valleys or depressions so that water-at-rest issues are not relevant.

Figure 5 shows the generic rectangular Monge domain used in all test cases. To implement our simulations, we employ the following boundary conditions: edges \overline{AB} , \overline{DC} and \overline{DA} are impermeable walls, while \overline{CB} represents the open outlet. In order to avoid the reflection of outgoing waves and discontinuous profiles at this latter boundary, a smooth transition of the bottom geometry is enforced at the outlet. The edge \overline{EF} describes the position of the initial water depth discontinuity, with upstream (shown with darker color in figure 5) and downstream depths of 2 m and 1 m, respectively. The same figure displays three uniformly distributed cross-sections $S_i, i = 1, 2, 3$ orthogonal to the lateral walls. These sections are used to evaluate streamflows. All the test cases consider the Gauckler-Strickler formula to describe the flow resistance at the bottom:

$$\tau_{b_i} = \frac{1}{k_s^2} \frac{u_i}{R_h^{4/3}}$$

with the resistance coefficient $k_s = 40 \text{ m}^{1/3}/\text{s}$.

The first test case considers sloping planes with variable inclinations to study the effects of small and large sloping angles on the dynamics of the flow. The second test case introduces simple one-dimensional curvatures on a sloping domain, and the last examines a fully three-dimensional bottom surface.

5.1. Test case 1: sloping planes.

This test case considers a rectangular Monge subset \mathcal{A} with the following dimensions: $\overline{AB}=10 \text{ m}$, $\overline{AD} = 1 \text{ m}$, $\overline{AF} = 1.40 \text{ m}$. Two sub-cases are defined by considering bottom surfaces with constant slopes of 5° and 25° , respectively. The discretization of \mathcal{A} is obtained with a Delaunay triangulation with average mesh

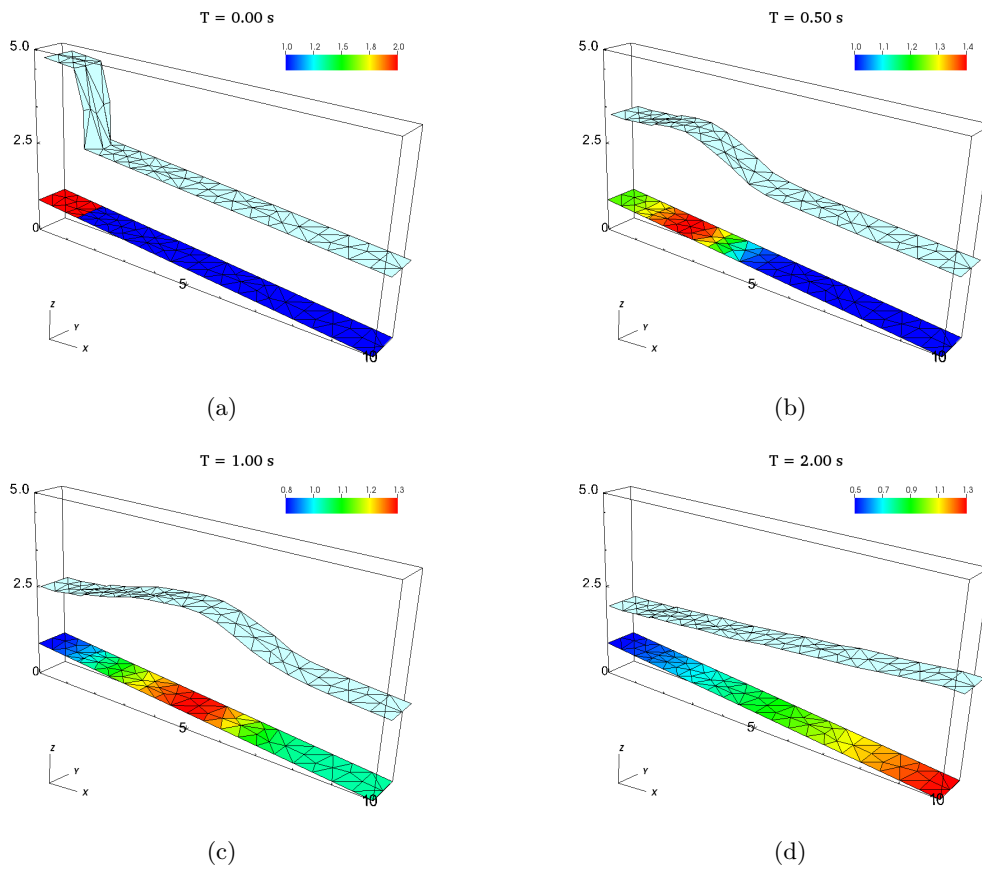


Figure 6: Test case 1: uniformly sloping bottom. Water depth [m] evolution of the simulation for the sub-case with 5° shown both as color codes and depth elevation, the latter with a magnification factor of 2.

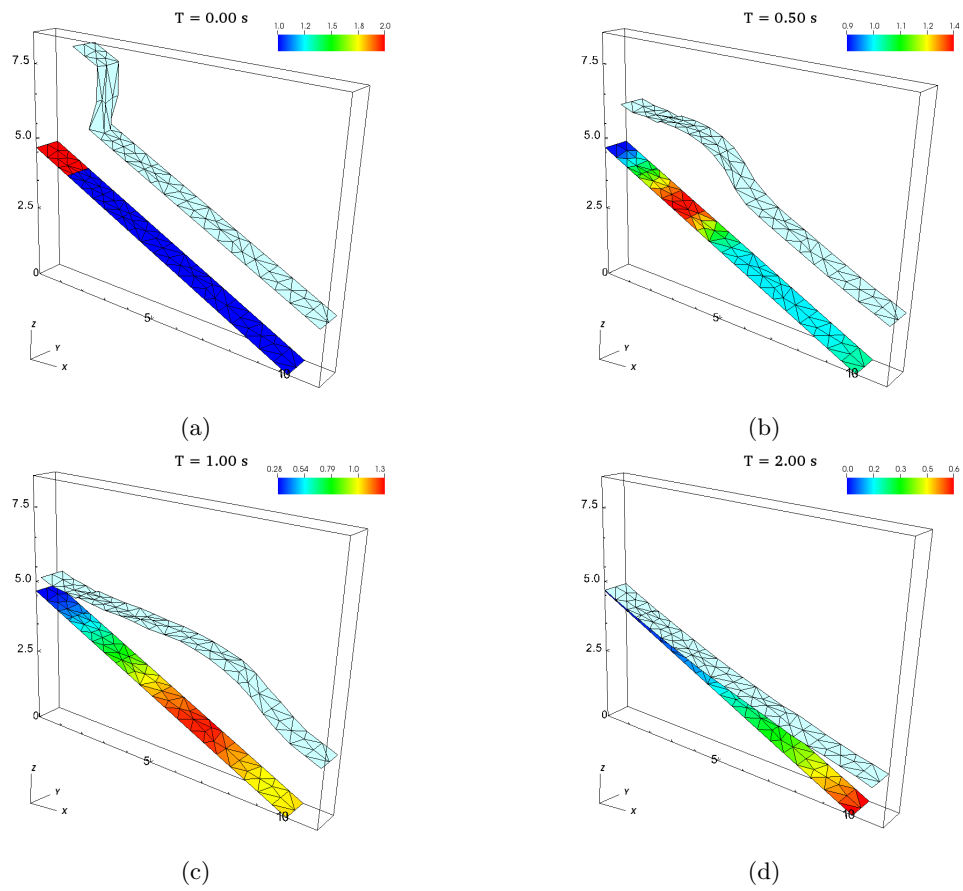


Figure 7: Test case 1: uniformly sloping bottom. Water depth [m] evolution of the simulation for the sub-case with 25° shown both as color codes and depth elevation, the latter with a magnification factor of 2.

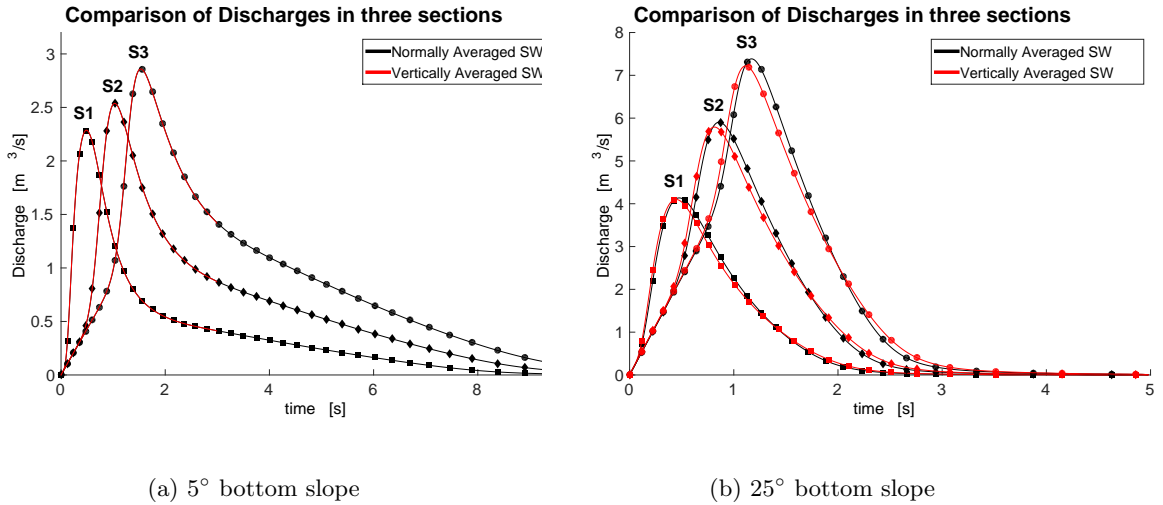


Figure 8: Test case 1: uniformly sloping bottom. Comparison of cross-sectional discharges computed in Sections S_1 , S_2 , and S_3 of figure 5 for different sloping angles and using the normally and vertically averaged SWE.

parameter $\ell=0.5$ m, yielding a total of 114 FV surface cells. Figures 6 and 7 show the numerically evaluated evolution of the gravity wave in terms of water depth η [m] at $t = 0.0$ s, 0.4 s, 0.8 s, and 1.2 s for the sub-case of 5° and 25°, respectively. The results show a non-oscillatory solution for both sub-cases with a strong numerical viscosity, typical of first order numerical schemes, that extends for more than three cells upstream and downstream the wave front. At the last time and for the largest slope sub-case, (figure 7d), the upstream portion of the domain reaches a dry state, without displaying numerical inconsistencies. Moreover, at the downstream boundary no backward waves are forming.

The quantitative differences between the results obtained with the normally averaged SWE and those obtained with the vertically averaged SWE approach are evaluated by looking at cross-sectional discharges passing through the three sections of figure 5. The results, reported in figure 8, show significant differences only for the largest slope sub-case (figure 8b), with increased peak discharge and a later time of arrival for the streamflows obtained from the normally averaged SWE. The total volumes, evaluated as the integrals under the curves, are the same for both vertically and normally averaged approaches, confirming that our FV method is conservative.

5.2. Test case 2: double parabola.

This test case aims at verifying the effects of curvatures for a simple one-dimensional propagation of the flow. Thus we consider a rectangular Monge subset \mathcal{A} with the same dimensions as in the previous test case. The Monge height function that describes the bottom surface is:

$$\mathcal{H}_B(x_1, x_2) = \begin{cases} -\frac{2}{25}x_1^2 + 4 & \text{if } x_1 \leq 5, \\ \frac{2}{25}(x_1 - 10)^2 & \text{otherwise.} \end{cases}$$

The discretization of \mathcal{A} is the same Delaunay triangulation with average mesh parameter $\ell = 0.5$ m, yielding a total of 114 FV surface cells. Initial conditions are the same as in test case 1.

Figure 9 reports the numerically evaluated evolution of the gravity wave in terms of water depth η [m] at $t = 0.33$ s, 0.50 s, 0.94 s, and 2.4 s. The wave moves slowly in the upper portion of the channel (figure 9a) and increases its speed approaching the steeper central portion (figure 9b). At around 0.33 s a new gravity wave forms in the domain center because of the acceleration induced by the change of bottom slope. Figure 9c shows that before $t \approx 1$ s the initial wave collapses on the tail of the later gravity wave, which is slowed down

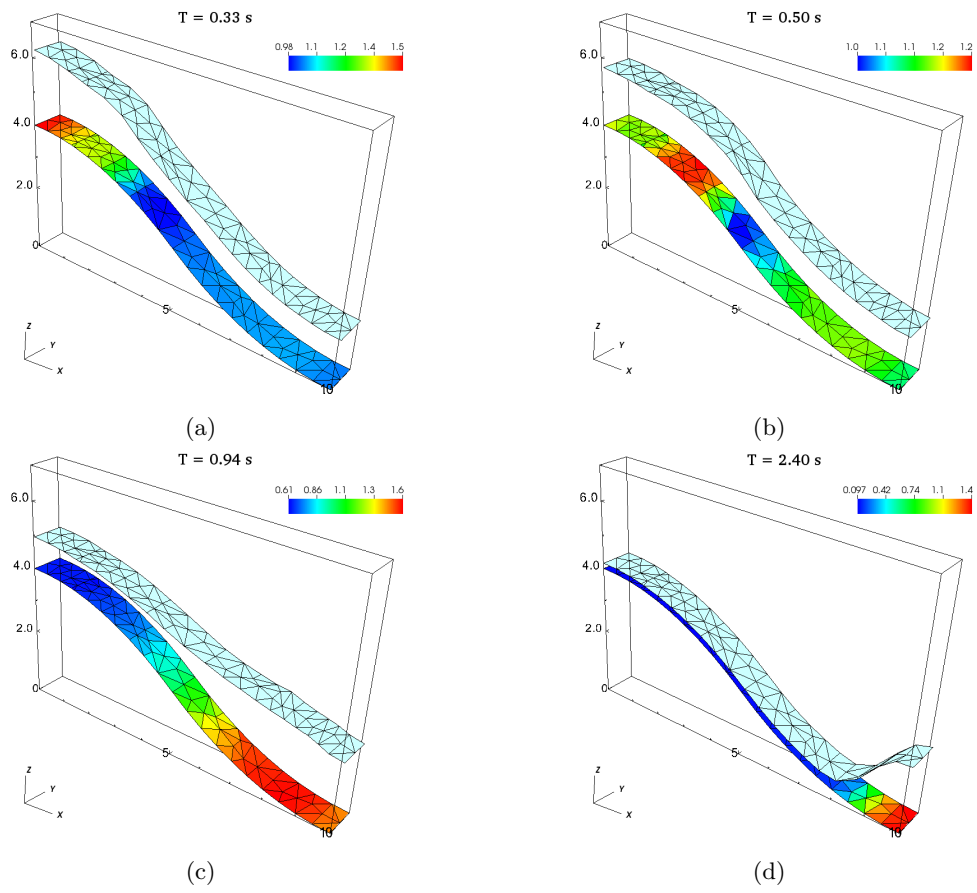


Figure 9: Test case 2: one-dimensional smooth curved bottom. Evolution of the gravity wave, shown both as color codes and depth elevation, the latter with a magnification factor of 1.5.

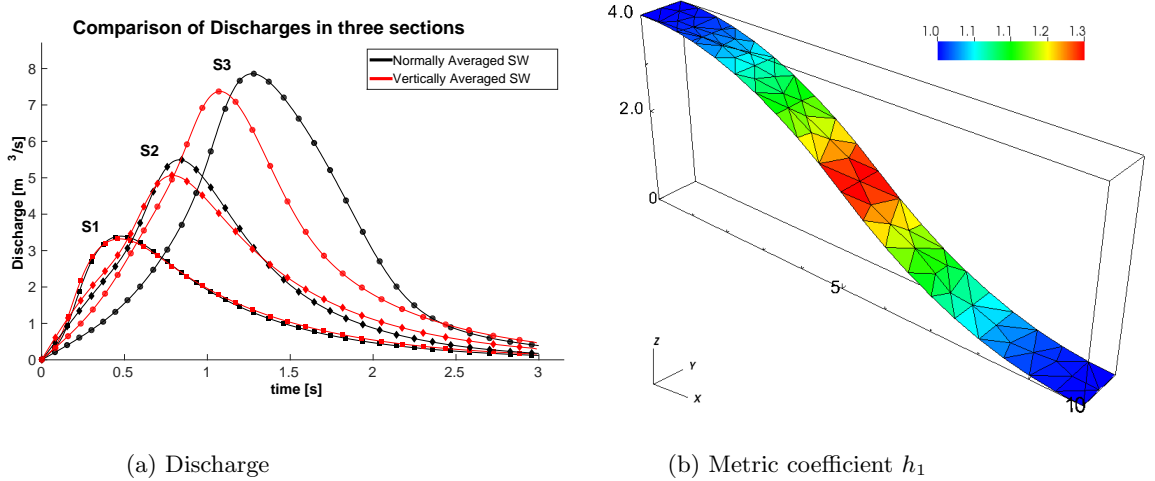


Figure 10: Test case 2: one-dimensional smooth curved bottom. Panel (a): comparison of discharges computed in the cross-sections S_1 , S_2 , S_3 , obtained from the normally and vertically averaged SWE. Panel (b): spatial distribution of the metric coefficient h_1

by the downstream decreasing bottom slope. This behavior is quantifiable by noticing that at $t = 0.33$ s the wave front is located at around 2 m from the upstream boundary, while at $t = 0.50$ s the same wave has traveled for around 2 m. On the other hand, in the next half a second ($t = 0.94$ s), the initial wave has traveled almost to the outlet. At the end of the simulation (figure 9d) most of the water volume has left the domain. Note that this occurs in a relatively long time, more than 1.5 s, because of the flatness of the downstream bottom topography.

Better appreciation of the influence of bottom geometry is achieved by comparing simulated discharges at the three channel cross sections, obtained by using normally and vertically averaged SWE. The results of this comparison are reported in figure 10a. The differences in the first section are rather small, a consequence of an almost flat topography upstream of S_1 . Much larger discrepancies are visible for the results of the other two sections, where higher discharge peaks and longer arrival times characterize the streamflow evaluated using the normally averaged model. This behavior can be attributed to the effects of the curvatures that cause lower discharge during the rising limb and a consequential later peak increase, so that mass conservation is satisfied. The effects of the bottom curvatures can be appreciated also by looking at the spatial distribution of the metric coefficient h_1 , reported in figure 10b. The largest values are localized in correspondence of section S_2 , which is where the concavity of the bottom topography changes. The presence of h_1 in the denominator of the terms of equation (15) contained in the divergence operator is responsible for local reductions of the conserved fluxes. These reductions are concentrated in the central portion of the domain, where the metric coefficient is largest.

In this test case we also evaluate the experimental convergence of the proposed FV scheme to verify its theoretical properties. To this aim, we look at norms of the differences between solutions at successively refined meshes and the solution obtained at the finest mesh. We use a rectangular domain of dimensionless length 1×0.1 , and the same “double-parabola” surface of Test case 2, scaled on this dimensionless domain. Then a sequence of uniform triangulations \mathcal{T}_ℓ is obtained by subdividing the domain in square cells, each one subdivided again into two triangles. The mesh levels are characterized by $\ell = 1/10, 1/20, 1/40, 1/80$. The solution obtained at $\ell = 1/80$ is used as reference solution, and is indicated with a tilde. Table 1 shows the L^2 and L^∞ norms of the errors evaluated on η and $|\mathbf{q}|$. The error norms decrease at a ratio that approaches the value 2, confirming that the proposed FV scheme is first order accurate.

ℓ	$\ \eta_\ell - \tilde{\eta}\ _2$	ratio	$\ \eta_\ell - \tilde{\eta}\ _\infty$	ratio
1/10	0.2560	-	0.1662	-
1/20	0.1951	1.312	0.1244	1.335
1/40	0.09766	1.998	0.07881	1.579
ℓ	$\ \mathbf{q}_\ell - \tilde{\mathbf{q}}\ _2$	ratio	$\ \mathbf{q}_\ell - \tilde{\mathbf{q}}\ _\infty$	ratio
1/10	1.684	-	0.9546	-
1/20	1.237	1.361	0.7982	1.196
1/40	0.7667	1.613	0.4042	1.975

Table 1: Test case 2: convergence of the proposed FV scheme. The errors are estimated by using the fine-grid ($\ell = 1/80$) solution $\tilde{\eta}$ and $|\tilde{\mathbf{q}}|$ as reference solution. The word “ratio” indicates the ratio between successive error norm estimates.

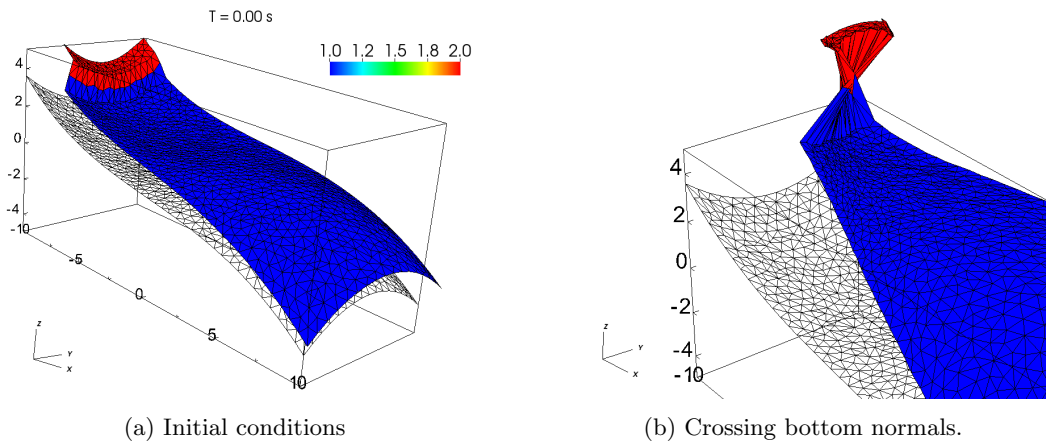


Figure 11: Test case 3: three-dimensional smooth curved bottom. Mesh and initial conditions (Panel 11a) for the test case problem defined on a fully three-dimensional surface. Panel 11b shows an example of the occurrence of singular points in the coordinate transformation, in the case of initial condition of 10 m upstream of the initial wave discontinuity.

5.3. Test case 3: three dimensional topography.

The final test case considers a fully three-dimensional surface, built starting from a rectangular Monge subset \mathcal{A} with the dimensions: $\overline{AB} = 20$ m, $\overline{AD} = 8$ m, $\overline{AF} = 1.50$ m. The Monge height function is given by:

$$\mathcal{H}_{\mathcal{B}}(x_1, x_2) = -\frac{1}{500}x_1^3 - \frac{1}{100}x_1x_2^2.$$

The final triangulation, shown in figure 11a, is characterized by an average mesh parameter $\ell = 0.5$ m, and a total of 1924 FV surface cells. The initial conditions (figure 11a) again consider a uniform water depth of 2 m upstream of $x_1 = -8.5$ m, and 1 m downstream. We would like to note that the choice of initial conditions of a 2 m deep reservoir avoids the singularities of the coordinate transformation by ensuring that water depth is sufficiently shallow so that bottom normals do not intersect within the fluid domain, as described in Section 2.2. For example, figure 11b shows what could happen had we chosen a water depth of 10 m in the reservoir. In this case the LCS cannot be used to perform the depth integration.

Initially, water waves propagate following the terrain shape. In the upper portion of the domain, water accumulates towards the center of the convex bowl forming a bell shaped wave and emptying the upper corners of the domain (figure 12b). At the same time, gravity waves form downstream, moving water laterally from the center towards the impermeable boundary walls. At $t = 1.90$ s (figure 12c) the upstream wave approaches the middle and almost flat section of the bottom surface occupying the entire width. The wave then progresses following the concavity of the bottom shape and leaves the domain through the open outlet, continuing the draining of the upstream fluid.

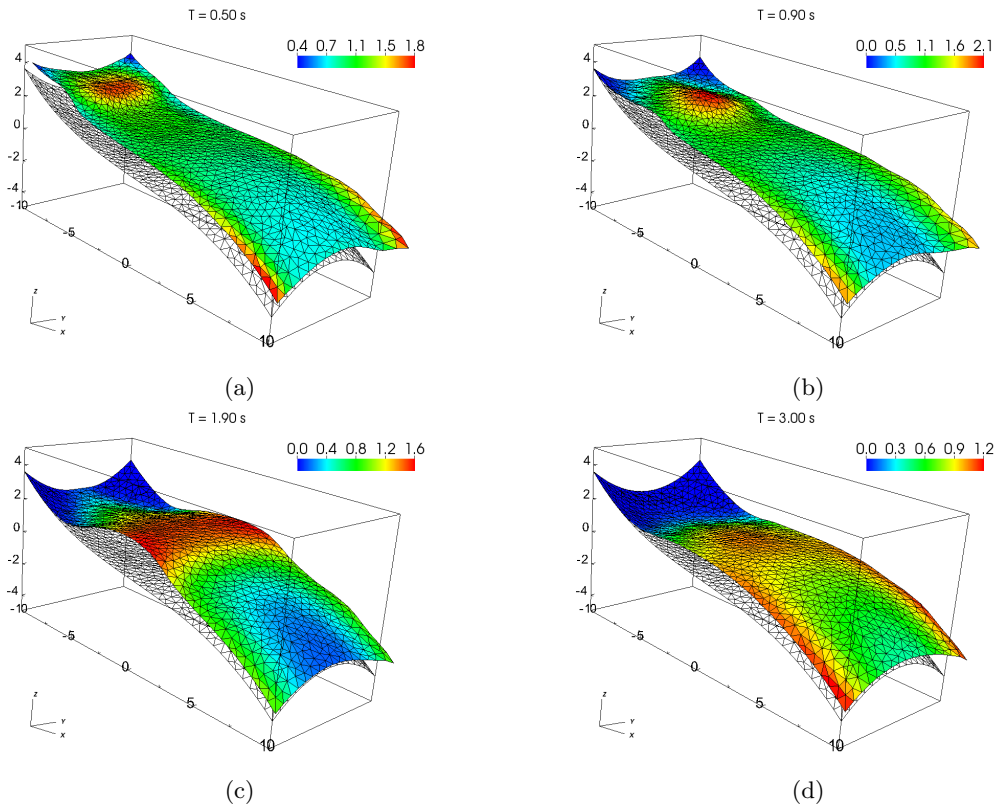


Figure 12: Test case 3: three-dimensional smooth curved bottom. Water depth [m] evolution of initial wave, shown both as color codes and depth elevation, the latter with a magnification factor of 1.3.

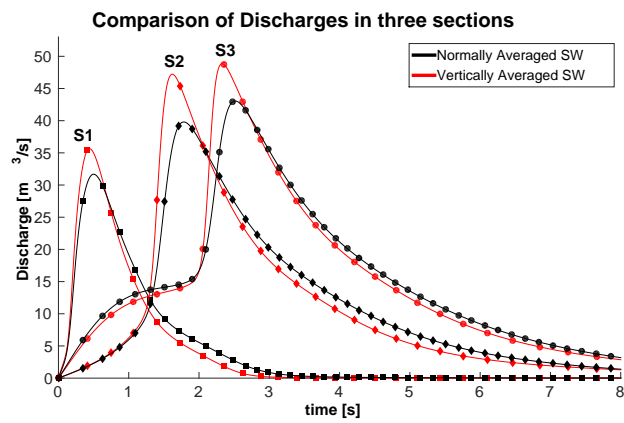


Figure 13: Test case 3: three-dimensional smooth curved bottom. Comparison of numerical discharges, obtained from the normally and vertically averaged SWE.

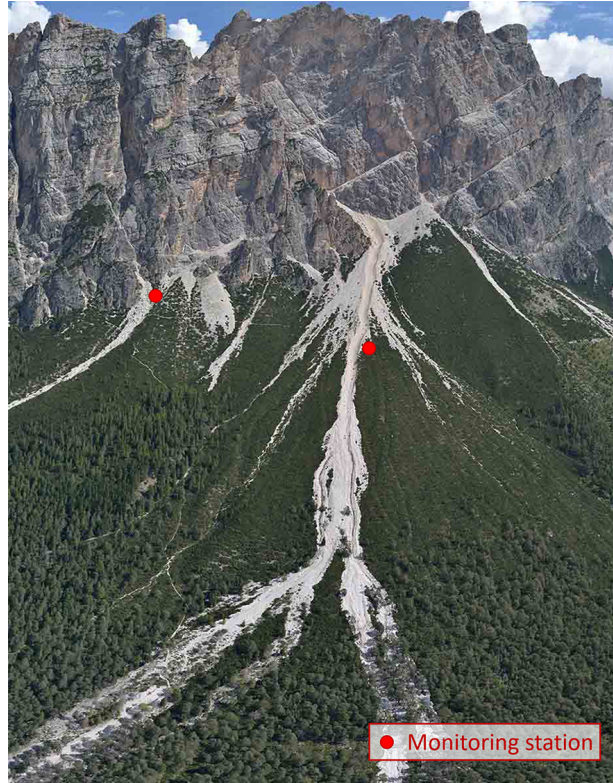


Figure 14: Example of complex terrain showing the instrumented debris flow experimental sites located in Fiammes (Dolomites), Northern Italy. Several other debris flow channels are clearly visible.

The behavior of the cross-sectional discharge as function of time differs drastically from the previous test cases as a consequence of a more complex bottom geometry, with all sections showing varied behavior (figure 13). We first notice that normally averaged discharges have lower peaks that arrive at slightly later times with respect to their vertically averaged counterparts. Again mass conservation is satisfied, with an observable delay of the volume arrivals. To verify the mass balance property, we have estimated the hydrograph volumes by evaluating the integral under the different curves by means of the Trapezoidal Rule. We obtained errors of the order of 6.4%, 1.8%, and 1.4% for Sections 1,2, and 3, respectively. Note that the reservoir volume is calculated following either the normal or the vertical direction, depending on the assumption. Thus error for Section 1, which is closer to the reservoir, is influenced by this discrepancy. The results, although no exact mass balance property can be proved for the FV scheme, seem to be sufficiently accurate and the differences decrease as the calculations progress. Focusing on single sections, we notice that section S_1 already shows important differences with a peak discharge discrepancy of around 10%. This is due to the influence of the metric coefficients that are active in both directions and throughout the entire domain. Section S_3 shows a peculiar behavior, with two waves clearly perceived: the initial rising limb of the curve is associated with the downstream gravity wave moving laterally and the following rising limb part corresponds to the arrival of the main water wave. Notice that, contrary to all the other curves, the normally averaged gravity wave precedes in time the corresponding vertically averaged wave. The 10% difference in the peak discharge is confirmed also for the last section.

5.4. Discussion of the results and future research

All these results show the importance of the effects of bottom geometry on the dynamics of the fluid movement, as governed by shallow water equations. Even in the presence of relatively mild curvatures,

significant differences with respect to the corresponding standard approach for SWE (i.e., derived by means of integration along the vertical direction) are correlated with the magnitude of the metric coefficients. Differences of around 20% are witnessed in several of the presented test cases, notwithstanding the smoothness and regularity of the three-dimensional surfaces employed in our simulations. This is a confirmation of the importance of the need to take into consideration geometrical effects of the bottom topography, in particular for real world application, where fluids move on generally rough terrains, as occurs, e.g., in mountainous areas. A typical example of the potential importance of bottom variations on the depth-averaged flow field is embodied by debris flows. This type of gravitational motions consist of a rapidly moving liquid-sediment mixture usually generated in narrow steep valleys, when loose masses of unconsolidated debris become unstable under the action of water supplied by rainfall or snow melting [63]. Due to inertia, the liquid-sediment mixture can travel for long distances and eventually deposit for low enough hillslopes, or when discharging in broad alluvial fans and in a less steep channel. The topography over which debris flows generate, propagate, and deposit is thus typically characterized by both relatively high slopes and highly variable curvatures, as can be intuitively observed from the photograph shown in figure 14 [64]. The present analysis suggests that a reliable estimate of the debris flow hydrograph requires that geometrical effects of the terrain over which the liquid-sediment mixture moves should be introduced in the depth-averaged models currently used to simulate this type of phenomena.

It is important to recognize the numerous assumptions that were made in the derivation of the normally averaged SWE on curvilinear local reference system. In particular, we would like to recall two important simplifications. The first is related to the choice of using the normal direction to approximate the cross-flow integration path. The influence of this assumption needs to be quantified, in relation to the hypothesis of linear pressure distribution along the different integration paths (along the vertical or normal directions or the cross-flow path). Techniques similar to those employed in [29] and [30] could be used in future work to assess these differences. The second important simplification is related to neglecting terms containing shear stress components comprising the differential advective terms as well as the turbulent and viscous stresses. These terms contain geometrical information which could alter their importance in case of large bottom curvatures. Disregarding these components, thus effectively incorporating their action into the uncertainty related to the empirical resistance coefficients, is then equivalent to a limitation on the admissible geometry of the bottom surface.

Future research will concentrate on studying these aspects in an attempt to contribute towards more accurate and robust simulations of geophysical flows. To this aim, geometrical effects of topography on beds formed by erodible sediments and, hence, of movable nature deserves attention in the near future.

6. Conclusions

The shallow water assumption, whereby horizontal variations of the flow field occur on much larger lengths than vertical variations, is widely adopted when deriving the depth-averaged equation used to model many natural phenomena. Usually, this derivation is carried out by integrating along the vertical the relevant three-dimensional mass and momentum conservation equations. However, the terrain over which the investigated flow fields often take place, is characterized by quite complex geometries, exhibiting non negligible bottom slopes (thus implying that the vertical direction does not approximate any more the normal to the bottom) and curvatures.

The present analysis addresses the solution of this problem by proposing the integration of the mass and momentum conservation equations along the local direction normal to the bottom surface. The geometry of this surface is defined using explicit mathematical expressions that facilitate the enucleation of the effects of curvatures on the flow dynamics. The results suggest that geometrical effects (embodied by the metric coefficients appearing into the final covariant form of the SWE equations) can significantly affect the flow field. In particular, the numerical simulations carried out on both uniformly sloping beds and synthetic but realistic smooth curved domains show that:

- the normally averaged SWE rather than the vertically averaged SWE need to be used for slopes larger than about 10% (as, e.g., those over which hyper-concentrated and debris flows occur);

- geometrical effects can be significant also for relatively mild and slowly varying curvatures. They affect both the peak values and the shape of the hydrograph at a given cross-section;
- the discretization of the proposed equations through a relatively simple first order FORCE-type Godunov finite volume scheme appears to ensure satisfactory results, achieving mass conservation and showing good stability properties even in the presence of flux functions that may be variable in space.

As stated explicitly in the introduction, our work addresses problems related to geophysical applications, where flow is no longer laminar and a solution in closed form for the base flow does not exist. We are specifically interested on the dynamics of long-waves determined by either non equilibrium of the initial conditions (e.g., a dam break) or temporal changes in the boundary conditions (e.g., variable input discharge or input/output water levels). In addition, the aim of our work is to develop a reduced dimensionality model that retains all the nonlinearities embodied by non linear advection and considers curvature effects on the flow forced by the bed topography, rather than in specifically modeling of the long waves that arise at the water surface as a consequence of flow instabilities (solitary pulses, roll waves) when the relevant flow parameters (e.g., the Froude number) attain some critical values. However, we conjecture that, in principle, these long waves can be described by our modelling approach once the full framework of integration along the cross-flow paths is developed.

Several improvements of the present modeling approach merit attention in the near future. On one hand, we would like to prove that our equations are an expansion of second order of a small parameter ϵ that takes into account the SW hypothesis of small vertical vs. horizontal scales and the geometric characteristics of the bottom surface, that the system is hyperbolic, admits a conserved energy in the absence of stresses, and is rotation invariant. This latter property is a fundamental requirement for a correct definition of the associated Riemann problem, so that upwind schemes can be developed. Also the fact that the fluxes are non-autonomous requires careful analytical studies, as well as the relaxation of the regularity assumptions on the solution deriving by the use of the chain rule of differentiation and Leibnitz theorem [50, 51, 60, 65]. Additionally, errors arising from the use of local bed normals to approximate the cross-flow integration path should be analyzed to arrive at corrections accounting for possible deviations from the assumed pressure distribution. Also well-balance properties and wetting and drying algorithms in the presence of a complex terrain should be suitably analyzed and tested. Improvements and advantages associated with the use of higher order numerical schemes also need to be considered. Errors involved in the evaluation of the geometrical quantities of the bottom surface need to be assessed in the case of bed geometry defined starting from measured data such as remotely sensed digital elevation maps.

Finally, the modelling of a movable bed, to take into account erosion and sedimentation, has to be properly addressed within the context of complex terrains to obtain robust and reliable predictions of natural phenomena as hyper-concentrated and debris flows. Future investigations will address possibly the sudden dynamic formation of channels incised on fans and the emergence of non-smooth bed geometries, whose numerical treatment is still an open issue [66].

7. Acknowledgments

We thank the anonymous reviewers for their helpful comments. This work was supported in part by the following projects: GAPDEMM “GIS- based integrated platform for Debris Flow Monitoring, Modeling and Hazard Mitigation” funded by CARIPARO foundation, the Multi-ITN EU-FP7 project SEDITRANS “Sediment transport in fluvial, estuarine and coastal environments”. All the three-dimensional figures were prepared using the VisIt High Performance visualization package [67].

References

- [1] R. L. Higdon, Numerical modelling of ocean circulation, *Acta Num.* 15 (2006) 385.
- [2] J. R. Holton, *An introduction to dynamic meteorology*, Burlington, MA: Elsevier Academic Press, 2004.
- [3] G. Zolezzi, G. Seminara, Downstream and upstream influence in river meandering. Part 1. General theory and application to overdeepening, *J. Fluid Mech.* 438 (2001) 183–211.

- [4] S. Lanzoni, A. Siviglia, A. Frascati, G. Seminara, Long waves in erodible channels and morphodynamic influence, *Water Resour. Res.* 42 (2006) W06D17.
- [5] L. Fraccarollo, H. Capart, Riemann wave description of erosional dam-break flows, *J. Fluid Mech.* 461 (2002) 1–46.
- [6] G. Rosatti, L. Begnudelli, Two dimensional simulations of debris flows over mobile beds: Enhancing the TRENT2D model by using a well-balanced generalized Roe-type solver., *Comput. Fluids* 71 (2013) 179–185, doi:doi10.1016/j.compfluid2012.10.006.
- [7] R. M. Iverson, D. L. George, A depth-averaged debris-flow model that includes the effects of evolving dilatancy. I. Physical basis, *Proc. R. Soc. Lond. A* 470 (2170) (2014) 20130819–20130819.
- [8] D. L. George, R. M. Iverson, A depth-averaged debris-flow model that includes the effects of evolving dilatancy. II. Numerical predictions and experimental tests, *Proc. R. Soc. Lond. A* 470 (2170) (2014) 20130820–20130820.
- [9] J. M. N. T. Gray, M. Wieland, K. Hutter, Gravity-driven free surface flow of granular avalanches over complex basal topography, *Phil. Trans. R. Soc. A* 455 (1985) (1999) 1841–1874.
- [10] A. Decoene, L. Bonaventura, E. Miglio, F. Saleri, Asymptotic derivation of the section-averaged shallow water equations for natural river hydraulics, *Math. Mod. Meth. Appl. Sci.* 19 (03) (2009) 387–417.
- [11] J. Pedlosky, *Geophysical fluid dynamics*, Springer Verlag, New York, 1979.
- [12] P. P. Jansen, L. van Bengedom, J. van den Berg, M. de Vries, A. Zanen, *Principles of river engineering: the non-tidal alluvial river*, Pittman, London, San Francisco, 1979.
- [13] V. T. Chow, *Open-channel hydraulics*, McGraw-Hill, New York, 1959.
- [14] A. S. Donahue, Y. Zhang, A. B. Kennedy, J. J. Westerink, N. Panda, C. N. Dawson, A Boussinesq-scaled, pressure-Poisson water wave model, *Ocean Model.* 86 (C) (2015) 36–57.
- [15] Y. Zhang, A. B. Kennedy, N. Panda, C. N. Dawson, J. J. Westerink, Boussinesq–Green–Naghdi rotational water wave theory, *Coast. Eng.* 73 (C) (2013) 13–27.
- [16] C. Aricò, C. Lo Re, A non-hydrostatic pressure distribution solver for the nonlinear shallow water equations over irregular topography, *Adv. Water Resources* 98 (2016) 47–69.
- [17] C. Ruyer-Quil, P. Manneville, Modeling film flows down inclined planes, *Eur. Phys. J. B* 6 (2) (1998) 277–292.
- [18] C. Ruyer-Quil, P. Manneville, Improved modeling of flows down inclined planes, *Eur. Phys. J. B* 15 (2) (2000) 357–369.
- [19] H. Tennekes, J. L. Lumley, *A First Course in Turbulence*, MIT Press, 1972.
- [20] V. Nikora, D. Goring, I. McEwan, Spatially averaged open-channel flow over rough bed, *J. Hydraul. Engrg. ASCE* 127 (2) (2001) 123–133.
- [21] T. Butler, L. Graham, D. Estep, C. Dawson, J. Westerink, Definition and solution of a stochastic inverse problem for the manning’s n parameter field in hydrodynamic models, *Adv. Water Resources* 78 (2015) 60–79.
- [22] S. B. Savage, K. Hutter, The motion of a finite mass of granular material down a rough incline, *J. Fluid Mech.* 199 (-1) (1989) 177–215.
- [23] S. B. Savage, K. Hutter, The dynamics of avalanches of granular materials from initiation to runout. Part I: Analysis, *Acta Mech.* 86 (1-4) (1991) 201–223.
- [24] F. Bouchout, M. Westdickenberg, Gravity driven shallow water models for arbitrary topography, *Comm. Math. Sci.* 2 (3) (2004) 359–389.
- [25] E. D. Fernández-Nieto, F. Bouchout, D. Bresch, M. J. Castro Díaz, A. Mangeney, A new Savage–Hutter type model for submarine avalanches and generated tsunamis, *J. Comp. Phys.* 227 (16) (2008) 7720–7754.
- [26] L. Moretti, K. Allstadt, A. Mangeney, Y. Capdeville, E. Stutzmann, F. Bouchout, Numerical modeling of the Mount Meager landslide constrained by its force history derived from seismic data, *J. Geophys. Res.* 120 (4) (2015) 2579–2599.
- [27] J. A. Rossmannith, D. S. Bale, R. J. LeVeque, A wave propagation algorithm for hyperbolic systems on curved manifolds, *J. Comp. Phys.* 199 (2) (2004) 631–662.
- [28] D. S. Bale, R. J. LeVeque, S. Mitran, J. A. Rossmannith, A wave propagation method for conservation laws and balance laws with spatially varying flux functions, *SIAM J. Sci. Comput.* 24 (3) (2002) 955–978.
- [29] M. Boutounet, L. Chupin, P. Noble, J. P. Vila, Shallow water viscous flows for arbitrary topography, *Comm. Math. Sci.* 6 (1) (2008) 29–55.
- [30] D. Bresch, P. Noble, Mathematical Derivation of Viscous Shallow-Water Equations with Zero Surface Tension, *Ind. Univ. Math. J.* 60 (4) (2011) 1137–1169.
- [31] P. Noble, J. P. Vila, Thin power-law film flow down an inclined plane: consistent shallow-water models and stability under large-scale perturbations, *J. Fluid Mech.* 735 (2013) 29–60.
- [32] C. Vreugdenhil, *Numerical Methods for Shallow-Water Flow*, Water Science and Technology Library, Springer Netherlands, ISBN 9780792331643, 1994.
- [33] H. Nakagawa, I. Nezu, *Turbulence in Open Channel Flows*, IAHR Monographs, Taylor & Francis, 1993.
- [34] D. Kim, P. Lynett, S. Socolofsky, A Depth-Integrated Model for Weakly Dispersive, Turbulent, and Rotational Fluid Flows, *Ocean Model.* 27 (2009) 198–214.
- [35] D.-H. Kim, P. J. Lynett, Turbulent mixing and passive scalar transport in shallow flows, *Phys. Fluids* 23 (1) (2011) 016603–17.
- [36] R. M. Iverson, R. P. Denlinger, Flow of variably fluidized granular masses across three-dimensional terrain 1. Coulomb mixture theory, *J. Geophys. Res.* 106 (B1) (2001) 537–552.
- [37] F. Gallerano, G. Cannata, Central WENO scheme for the integral form of contravariant shallow-water equations, *International Journal for Numerical Methods in Fluids* 67 (8) (2011) 939–959.
- [38] F. Gallerano, G. Cannata, M. Tamburrino, Upwind WENO scheme for shallow water equations in contravariant formulation, *Computers & Fluids* 62 (2012) 1–12.
- [39] F. Bouchout, Nonlinear Stability of Finite Volume Methods for Hyperbolic Conservation Laws, And Well-Balanced Schemes

for Sources, Springer Science & Business Media, 2004.

- [40] G. Dziuk, C. M. Elliott, Finite element methods for surface PDEs, *Acta Numerica* 22 (2013) 289–396.
- [41] A. Canestrelli, M. Dumbser, A. Siviglia, E. F. Toro, Well-balanced high-order centered schemes on unstructured meshes for shallow water equations with fixed and mobile bed, *Adv. Water Resources* 33 (3) (2010) 291–303, doi:http://dx.doi.org/10.1016/j.advwatres.2009.12.006.
- [42] A. Canestrelli, S. Fagherazzi, S. Lanzoni, A mass-conservative centered finite volume model for solving two-dimensional two-layer shallow water equations for fluid mud propagation over varying topography and dry areas, *Adv. Water Resources* 40 (2012) 54–70.
- [43] G. Batchelor, *An Introduction to Fluid Dynamics*, Cambridge Mathematical Library, Cambridge University Press, ISBN 9780521663960, 2000.
- [44] M. Abate, F. Tovena, *Curves and Surfaces*, Springer-Verlag Italia, Milano, Italy, 2012.
- [45] M. P. Do Carmo, *Differential Geometry of Curves and Surfaces*, Prentice-Hall, Englewood Cliffs, New Jersey, 1976.
- [46] L. Balsemin, *Shallow Water Model of Flow on a General Topography*, Ms thesis, Dept. of Mathematics, University of Padova, Italy, 2015.
- [47] K. Hutter, Y. Wang, S. P. Pudasaini, The Savage–Hutter avalanche model: how far can it be pushed?, *Phil. Trans. R. Soc. A* 363 (1832) (2005) 1507–1528.
- [48] G. B. Folland, *Introduction to Partial Differential Equations*, Princeton University Press, New Jersey, USA, 1995.
- [49] W. M. Boothby, *An introduction to differentiable manifolds and Riemannian geometry*; 2nd ed., *Pure Appl. Math.*, Academic Press, Orlando, FL, 2003.
- [50] G. Crasta, V. De Cicco, A Chain Rule Formula in the Space BV and Applications to Conservation Laws, *SIAM J. Matrix Anal.* 43 (1) (2011) 430–456.
- [51] L. Ambrosio, G. Crasta, V. De Cicco, G. De Philippis, A nonautonomous chain rule in $W_{1,p}$ and BV , *Manuscripta Math.* 140 (3-4) (2012) 461–480.
- [52] H. D. Schlichting, K. Gersten, *Boundary-Layer Theory*, Springer-Verlag Berlin Heidelberg, ninth edition edn., ISBN 978-3-662-52917-1, 2017.
- [53] A. Frascati, S. Lanzoni, A mathematical model for meandering rivers with varying width, *J. Geophys. Res.* 118 (2013) 164101657.
- [54] R. J. Leveque, *Finite Volume Methods for Hyperbolic Problems*, Cambridge University Press, Trumpington Street, Cambridge, UK, 2002.
- [55] E. F. Toro, A. Hidalgo, M. Dumbser, FORCE schemes on unstructured meshes I: Conservative hyperbolic systems, *J. Comp. Phys.* 228 (2009) 3368–3389, doi:10.1016/j.jcp.2009.01.025.
- [56] A. Mazzia, G. Manzini, M. Putti, Bad behavior of Godunov mixed methods for strongly anisotropic advection-dispersion equations, *J. Comp. Phys.* 230 (2) (2011) 8410–8426.
- [57] D. S. Kershaw, Differencing of the diffusion equation in Lagrangian hydrodynamic codes, *J. Comp. Phys.* 39 (2) (1981) 375–395.
- [58] A. Kurganov, S. Noelle, G. Petrova, Semidiscrete Central-Upwind Schemes for Hyperbolic Conservation Laws and Hamilton–Jacobi Equations, *SIAM J. Sci. Comput.* 23 (3) (2001) 707–740.
- [59] M. J. Castro Díaz, C. Parés, G. Puppo, G. Russo, Central Schemes for Nonconservative Hyperbolic Systems, *SIAM J. Sci. Comput.* 34 (5) (2012) B523–B558.
- [60] B. Andreianov, K. H. Karlsen, N. H. Risebro, A Theory of L_1 -Dissipative Solvers for Scalar Conservation Laws with Discontinuous Flux, *Arch. Rational Mech. Anal.* 201 (1) (2011) 27–86.
- [61] J.-M. Morvan, *Generalized Curvatures*, vol. 2 of *Geometry and Computing*, Springer Science & Business Media, Berlin, Heidelberg, 2008.
- [62] G. Dal Maso, P. G. Lefloch, F. Murat, Definition and weak stability of nonconservative products, *J. Math. Pure Appl.* 74 (6) (1995) 483–548.
- [63] T. Takahashi, *Debris Flows: Mechanics, Prediction and Countermeasures*, Taylor & Francis, London, New York, 2007.
- [64] C. Gregoretto, M. Degetto, M. Bernard, G. Crucil, A. Pimazzoni, G. De Vido, M. Berti, A. Simoni, S. Lanzoni, Runoff of small rocky headwater catchments: Field observations and hydrological modeling, *Water Resour. Res.* 52 (10) (2016) 8138–8158.
- [65] L. Ambrosio, N. Fusco, D. Pallara, *Functions of bounded variation and free discontinuity problems*, vol. 254, Clarendon Press Oxford, 2000.
- [66] A. Valiani, V. Caleffi, Momentum balance in the shallow water equations on bottom discontinuities, *Adv. Water Resources* 100 (C) (2017) 1–13.
- [67] H. Childs, E. Brugger, B. Whitlock, J. Meredith, S. Ahern, D. Pugmire, K. Biagas, M. Miller, C. Harrison, G. H. Weber, H. Krishnan, T. Fogal, A. Sanderson, C. Garth, E. W. Bethel, D. Camp, O. Rübel, M. Durant, J. M. Favre, P. Navrátil, VisIt: An End-User Tool For Visualizing and Analyzing Very Large Data, in: *High Performance Visualization—Enabling Extreme-Scale Scientific Insight*, 357–372, 2012.